

# A current density conservative scheme for incompressible MHD flows at a low magnetic Reynolds number. Part I: On a rectangular collocated grid system

Ming-Jiu Ni <sup>a,c,\*</sup>, Ramakanth Munipalli <sup>b</sup>, Neil B. Morley <sup>a</sup>,  
Peter Huang <sup>b</sup>, Mohamed A. Abdou <sup>a</sup>

<sup>a</sup> MAE Department, University of California at Los Angeles, CA 90095, USA

<sup>b</sup> HyperComp Inc., Westlake Village, CA 91362, USA

<sup>c</sup> Physics Department, Graduate University of Chinese Academy of Sciences, Beijing 100049, China

Received 7 August 2006; received in revised form 16 April 2007; accepted 22 July 2007

Available online 9 August 2007

---

## Abstract

A consistent, conservative and accurate scheme has been designed to calculate the current density and the Lorentz force by solving the electrical potential equation for magnetohydrodynamics (MHD) at low magnetic Reynolds numbers and high Hartmann numbers on a finite-volume structured collocated grid. In this collocated grid, velocity ( $\mathbf{u}$ ), pressure ( $p$ ), and electrical potential ( $\phi$ ) are located in the grid center, while current fluxes are located on the cell faces. The calculation of current fluxes on the cell faces is conducted using a conservative scheme, which is consistent with the discretization scheme for the solution of electrical potential Poisson equation. A conservative interpolation is used to get the current density at the cell center, which is used to conduct the calculation of Lorentz force at the cell center for momentum equations. We will show that both “conservative” and “consistent” are important properties of the scheme to get an accurate result for high Hartmann number MHD flows with a strongly non-uniform mesh employed to resolve the Hartmann layers and side layers of Hunt’s conductive walls and Shercliff’s insulated walls. A general second-order projection method has been developed for the incompressible Navier–Stokes equations with the Lorentz force included. This projection method can accurately balance the pressure term and the Lorentz force for a fully developed core flow. This method can also simplify the pressure boundary conditions for MHD flows.

© 2007 Elsevier Inc. All rights reserved.

*Keywords:* Consistent and conservative scheme; Projection method; MHD

---

DOI of original article: [10.1016/j.jcp.2007.07.023](https://doi.org/10.1016/j.jcp.2007.07.023)

\* Corresponding author. Address: Physics Department, Graduate University of Chinese Academy of Sciences, Beijing 100049, China.

E-mail addresses: [mjni@gucas.ac.cn](mailto:mjni@gucas.ac.cn), [mjni@ucla.edu](mailto:mjni@ucla.edu) (M.-J. Ni).

URL: [www.fusion.ucla.edu](http://www.fusion.ucla.edu) (M.A. Abdou).

### 1. Introduction

Magnetohydrodynamic (MHD) flow at high Hartmann numbers has been a topic of great interest in the development of a fusion reactor blanket [1,2]. The self-cooled liquid–metal blanket [3] and dual coolant lead lithium [4] uses liquid lithium or the eutectic alloy Pb–17Li as the coolant as well as the breeding material. To design such liquid metal based blankets for fusion reactors, one must know the characteristics of MHD flows at high Hartmann numbers, such as the high MHD pressure drop and effects on flow profiles [5].

Two-dimensional MHD channel flows have been extensively studied by theoretical analysis and numerical simulation [6–9]. The square of the Hartmann number  $Ha$  is the ratio between the electromagnetic and the viscous forces. It is therefore a measure of the magnetic field strength for a given fluid in a duct of a given scale. The thickness of the Hartmann layers scales with  $Ha^{-1}$  and is very thin; the side layers parallel to the magnetic field scale with  $Ha^{-1/2}$  and are much thicker than the Hartmann layers at high Hartmann numbers. The development of fusion reactors experiments with strong magnetic fields leads to a growing interest in the study of 3D MHD phenomena. When inertial terms are small, the asymptotic method [10–12] that focuses on the main phenomena is a very efficient method to compute 3D MHD flows. This efficient method is valid for high Hartmann numbers and high interaction parameters. When inertial terms are important, the direct simulation method accounting for all the physical effects is an important tool to study the 3D MHD phenomena. Using the direct simulation method, a very fine mesh is required to resolve the Hartmann layer and the side layer at high Hartmann numbers. For unsteady flows, the time step is proportional to the smallest grid size with an explicit update of the temporal term. The cost of direct simulation of 3D MHD flows at high Hartmann number is high since it requires a fine mesh and therefore a small time step for unsteady flows. Three-dimensional numerical simulations of inertial flows are often limited to the steady regime and low Hartmann numbers.

For low magnetic Reynolds numbers, the electrical potential formula can be employed for MHD with good accuracy [13–15]. For incompressible liquid fluid flow, a staggered grid system is usually employed to efficiently avoid the checkerboard phenomenon of pressure. When this grid system is applied for low magnetic Reynolds number, the pressure and electrical potential can be put at the cell center point as shown in Fig. 1a. Sterl [16] conducted a direct numerical simulation of liquid metal MHD flows in rectangular ducts using a uniform mesh. Usually it is not difficult to design a conservative scheme for MHD calculation on a uniform mesh. However, requiring 2–3 grids inside the Hartmann layer and the side layer will greatly increase the computational time on a uniform mesh as Hartmann number increases. In Sterl’s calculation, Hartmann number is limited to less than 1000 for 2D cases and to less than 50 for 3D cases. For fusion blankets, Hartmann number can be as high as  $10^4$ – $10^5$ , and non-uniform grids are needed to improve the computational efficiency. Leboucher [17] found that the classical second-order difference scheme for electrical potential gradient cannot ensure a good solution for side layers on a non-uniform mesh based on an ordinary staggered grid system (see Fig. 1a). Leboucher attributes this to the larger leading error terms. He noted in [17] that a numerically stable scheme for  $(\mathbf{u} \times \mathbf{B}) \times \mathbf{B} = B^2 \mathbf{u}_\perp$  is inaccurate when used together with  $\nabla\varphi \times \mathbf{B}$  the Lorentz force term discretized on an ordinary staggered grid.  $\mathbf{u}_\perp$  is the velocity component normal to the applied magnetic field direction. The derivative  $\partial\varphi/\partial z$  involved in the term  $\nabla\varphi \times \mathbf{B}$  needs to be known at the grid point  $(i + \frac{1}{2}, j, k)$  before it is added to the  $x$ -component of the momentum equation. It is interesting to note the difference between the following two formulas:

- Formula of  $\partial\varphi/\partial z$  based on four-point discretization:

$$\left(\frac{\partial\varphi}{\partial z}\right)_{i+\frac{1}{2},j,k} = \frac{1}{2} \left( \frac{\varphi_{i,j,k+1} - \varphi_{i,j,k-1}}{z_{k+1} - z_{k-1}} + \frac{\varphi_{i+1,j,k+1} - \varphi_{i+1,j,k-1}}{z_{k+1} - z_{k-1}} \right) \tag{1}$$

- Formula of  $\partial\varphi/\partial z$  based on six-point discretization:

$$\left(\frac{\partial\varphi}{\partial z}\right)_{i+\frac{1}{2},j,k} = \frac{1}{4} \left( \frac{\varphi_{i,j,k+1} - \varphi_{i,j,k}}{z_{k+1} - z_k} + \frac{\varphi_{i,j,k} - \varphi_{i,j,k-1}}{z_k - z_{k-1}} \right) + \frac{1}{4} \left( \frac{\varphi_{i+1,j,k+1} - \varphi_{i+1,j,k}}{z_{k+1} - z_k} + \frac{\varphi_{i+1,j,k} - \varphi_{i+1,j,k-1}}{z_k - z_{k-1}} \right) \tag{2}$$

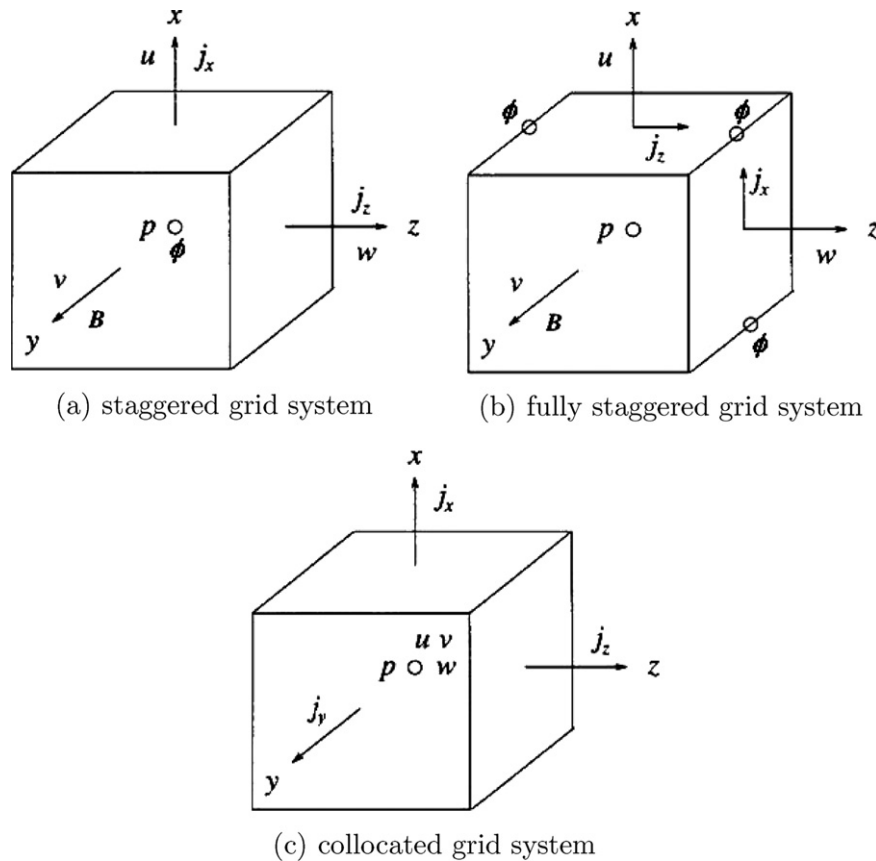


Fig. 1. Three grid arrangement systems.

On a uniform mesh, the above formulas are equivalent. However, on a non-uniform mesh, the above two formulas are entirely different. Fig. 2 is an illustrated non-uniform mesh generated for the simulation of Hunt's case with Hartmann number 10,000. The maximum grid size ratios in  $y$  and  $z$  directions are  $\Delta y_{\max}/\Delta y_{\min} = 10,000$  and  $\Delta z_{\max}/\Delta z_{\min} = 1000$ , respectively. With a non-uniform mesh employed, we will show later that Eq. (1) is neither conservative nor consistent, while Eq. (2) is conservative and consistent with respect to the calculation of current density. The non-conservative and inconsistent formula will definitely introduce an error into the calculation of current density. The accuracy and conservative properties of discretized schemes on a uniform mesh is discussed in [18]. A series of energy conservative schemes are constructed for the convective term and pressure term of the Navier–Stokes equations. The energy conservative scheme is also discussed and constructed on a non-uniform mesh in [19] and unstructured staggered mesh in [20] and unstructured collocated mesh in [21]. The energy conservative scheme has great advantages over a non-conservative scheme in the DNS and LES for turbulent flows [18]. However, in this paper, we will discuss and develop a consistent and conservative scheme for the calculation of the current density and the Lorentz force for MHD flows.

To keep a scheme consistent and conservative, a fully staggered grid system is designed in [17] for MHD calculation with high Hartmann number as shown in Fig. 1b. Velocities and current fluxes are arranged on the cell faces and pressure is arranged at the node center, while the electrical potential is arranged at the edge centers of a cell box. Leboucher [17] even puts the current flux of  $j_x$  at the center of the  $xy$  cell face,  $j_z$  at the center of the  $yz$  cell face. He did not mention the arrangement of  $j_y$  for his 2D calculation or 3D calculation with a unidirectional fixed applied magnetic field. This arrangement adds numerical complexity, especially for three-dimensional simulation on a finite-volume unstructured mesh with multi-directional applied magnetic field. We also note that this fully staggered grid system has been applied in [22] to conduct LES (large eddy

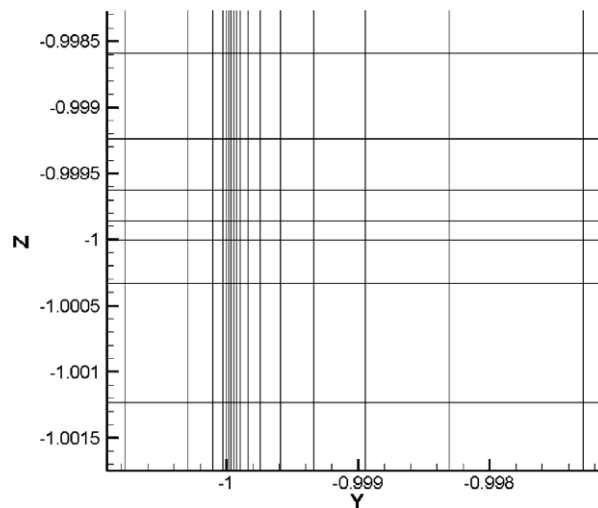


Fig. 2. Non-uniform grids generated for  $Ha = 10,000$ .

simulation) of turbulent MHD. Umeda and Takahashi [23] employed a fully staggered grid to simulate MHD flows for fusion application.

A collocated grid system has been employed for MHD simulations [24–26] based on the commercial CFD (computational fluid dynamics) software CFX [27]. However the scheme used in [24,25] is neither consistent nor conservative with respect to current density. In [26], it has been noted that a consistent scheme used to calculate the current related to  $\mathbf{u} \times \mathbf{B}$  is important. However, the Lorentz force calculated at the cell center is not based on a conservative formula. In [24,25], the simulation for fully developed MHD channel flow ( $Ha = 1000$ ) shows a large difference between their numerical method and analytical results. Also, Ref. [26] can only illustrate results for low Hartmann numbers.

In this paper, an accurate, consistent and conservative scheme is designed on a collocated grid system to calculate the current density and the Lorentz force for MHD flows at low magnetic Reynolds number with the electrical potential formulation. In this scheme, velocities, pressure and electrical potential are computed at the cell center. Velocity fluxes at the cell faces are calculated based on a momentum interpolation [28,29] to avoid checkerboard phenomena. The current density fluxes are located on the cell faces, and a consistent scheme is used to get the current fluxes on the cell faces to ensure the divergence-free current in a controlled volume. A conservative interpolation technique is used to get the current density at the cell center by interpolating the conservative current fluxes. This arrangement effectively avoids the numerical instability of regular schemes, and has good conservation with respect to the current density at the side layer and the Hartmann layer. This scheme has already been extended on an unstructured grid system [30] with a conservative formula employed to conduct the calculation of Lorentz force at the cell center.

A general second-order temporally accurate projection method [31] has been extended for incompressible Navier–Stokes equations with the Lorentz force as a source term. This projection method can accurately and effectively balance the pressure term and Lorentz force in the fully developed core flow. This projection method can also simplify the pressure boundary conditions for MHD flows. This general projection method can be reduced to the classical projection methods, such as the method in [32,33]. Also the SIMPLE-type methods, such as the standard SIMPLE method in [34,35] and the SIMPLEC method in [36], can be acquired from the general projection method.

The general projection method is developed for MHD in Section 2. Section 3 gives the detailed description of the consistent and conservative method developed for the calculation of current density and the Lorentz force. In Section 4, several numerical experiments are conducted. The comparisons between consistent and inconsistent formulas and between conservative and non-conservative schemes are analyzed. Numerical results will show that the conservative and consistent method developed in this paper can accurately simulate MHD at high Hartmann numbers.

## 2. General second-order projection method for MHD flows

The flow of electrically conducting fluid under the influence of an external magnetic field is governed by the following equations, which express the conservation of momentum and mass:

$$\frac{\partial \mathbf{u}}{\partial t} + \mathbf{u} \cdot \nabla \mathbf{u} = -\nabla p + \frac{1}{Re} \nabla^2 \mathbf{u} + N(\mathbf{J} \times \mathbf{B}) \quad (3)$$

$$\nabla \cdot \mathbf{u} = 0 \quad (4)$$

where  $\mathbf{u}$ ,  $p$  are the non-dimensional velocity vector and kinetic pressure scaled with  $u_0$  and  $\rho u_0^2$ , respectively. With  $L$  defined as characteristic length,  $Re = u_0 L / \eta$  is the Reynolds number,  $Ha = LB_0 \sqrt{\sigma / \rho \eta}$  is the Hartmann number, and  $N = Ha^2 / Re$  is the interaction parameter.  $\mathbf{J}$  represents the current density, and  $\mathbf{B}$  is the applied magnetic field scaled with  $\sigma u_0 B_0$  and  $B_0$ , respectively. Also we define the magnetic Reynolds number here as  $Re_m = \mu \sigma L u_0$ , where  $\eta$  and  $\sigma$  are the fluid viscosity and conductivity, respectively.  $\mu$  is the permeability of the fluid and the walls,  $\rho$  is the density of the fluid. The term  $N(\mathbf{J} \times \mathbf{B})$  is the Lorentz force, which is a volume force in a non-conservative form in the momentum equation of (3).

### 2.1. Balance between pressure gradient and the Lorentz Force

In the situation where  $N$  is large, we have an approximation known as fully developed core flow and Eq. (3) can be reduced to:

$$\nabla p = N(\mathbf{J} \times \mathbf{B}) \quad (5)$$

where the Lorentz force will balance the pressure gradient. Considering a fully developed MHD flow in a rectangular channel, with flow velocity in the  $x$ -direction, all derivatives with respect to  $x$  are zero except for that of pressure, which is a constant along the flow and zero in solid regions. An applied magnetic field is assumed in the  $y$ -direction and the magnetic Reynolds number is assumed to be small so that an electric potential formulation can be used. Electric current is computed from Ohm's law as:

$$\mathbf{J} = (0, j_y, j_z) = \sigma \left( 0, -\frac{\partial \varphi}{\partial y}, -\frac{\partial \varphi}{\partial z} + u \right) \quad (6)$$

In the core of the flow the balance Eq. (5) leads to the following relations:

$$-\frac{\partial \varphi}{\partial z} + u = \frac{Re}{Ha^2} \frac{dp}{dx} \quad (7)$$

At high  $Ha$  (therefore, high interaction parameter  $N$ ) with a given pressure gradient which corresponds to a given flow rate, the right hand side of the above equation is very small. The core dimensionless velocity being close to 1, we require the dimensionless gradient of the electric potential above to be also close to 1 in magnitude, but opposite in sign. We then have a situation in which current is computed from the difference between two (nearly identical) large numbers. It turns out that this imposes some restrictions on the manner in which current is numerically computed from the electric potential. The first issue is that of formal order of accuracy. Second, there is some reason to believe that leading truncation error terms in Taylor expansions of the two terms in Ohm's law, the potential gradient and the  $\mathbf{u} \times \mathbf{B}$  terms, in the numerical calculation of current may cause accumulation of error in a collocated sense, while they may effectively annul each other when staggered appropriately, as observed by Leboucher [17]. The consistent and conservative scheme designed in this paper attempts to alleviate these concerns for a collocated grid system.

### 2.2. Two four-step projection methods and boundary conditions for MHD flows

Before discussing the consistent and conservative scheme for the calculation of the current density and the Lorentz force in Section 3, we first develop a general projection method for the incompressible Navier–Stokes equations with the Lorentz force included. An accurate projection method should be able to enforce the balance between the pressure gradient and the Lorentz force for a fully developed core flow. For the

incompressible momentum and mass conservative equations (3) and (4) with the Lorentz force taken into account, the four-step general second-order projection method [31] can be extended as:

- Four-step projection method I

$$A\hat{\mathbf{u}} = \mathbf{r}^k + \mathbf{G}p^k + N(\mathbf{J} \times \mathbf{B})^k \tag{8}$$

$$\tilde{\mathbf{u}} = \hat{\mathbf{u}} + \Delta t(\Theta_p^k \mathbf{G}p^k - \Theta_F^k N(\mathbf{J} \times \mathbf{B})^k) \tag{9}$$

$$\Delta t \mathbf{D}(\Theta_p^k \mathbf{G}p^{k+1}) = \mathbf{D}(\tilde{\mathbf{u}} + \Delta t \Theta_F^k N(\mathbf{J} \times \mathbf{B})^{k+1}) \tag{10}$$

$$\mathbf{u}^{k+1} = \tilde{\mathbf{u}} - \Delta t(\Theta_p^k \mathbf{G}p^{k+1} - \Theta_F^k N(\mathbf{J} \times \mathbf{B})^{k+1}) \tag{11}$$

- Four-step projection method II

$$A\hat{\mathbf{u}} = \mathbf{r}^k + \mathbf{G}p^k + N(\mathbf{J} \times \mathbf{B})^k \tag{12}$$

$$\tilde{\mathbf{u}} = \hat{\mathbf{u}} + \Delta t \Theta_p^k \mathbf{G}p^k \tag{13}$$

$$\Delta t \mathbf{D}(\Theta_p^k \mathbf{G}p^{k+1}) = \mathbf{D}(\tilde{\mathbf{u}}) \tag{14}$$

$$\mathbf{u}^{k+1} = \tilde{\mathbf{u}} - \Delta t \Theta_p^k \mathbf{G}p^{k+1} \tag{15}$$

where  $A$ ,  $\mathbf{G}$ , and  $\mathbf{D}$  are submatrices,  $\mathbf{D}$  is the discrete divergence operator, and  $\mathbf{G}$  is the discrete gradient operator. The right-hand-side  $\mathbf{r}$  vector contains all those quantities that are already known except the Lorentz force. Explicitly updating the convective term for simplicity and performing semi-implicit Crank-Nicholson updating of the diffusion term for stability, we have  $\mathbf{r} = \frac{1}{\Delta t}(\mathbf{I} + \frac{\Delta t}{2Re}\mathbf{L})\mathbf{u}^k - \mathbf{NC}^{k+1/2}(\mathbf{u})$  and  $A = \frac{1}{\Delta t}(\mathbf{I} - \frac{\Delta t}{2Re}\mathbf{L})$ . Here  $\mathbf{L}$  is a discretized Laplace operator and  $\mathbf{NC}^{k+1/2}(\mathbf{u})$  is the sum of the discrete convective operator.  $\mathbf{I}$  is the unit identity matrix operator,  $\Theta_p = (\theta_{px}, \theta_{py}, \theta_{pz})$  and  $\Theta_F = (\theta_{Fx}, \theta_{Fy}, \theta_{Fz})$  are the diagonal coefficient matrices with elements of  $\theta_{px}, \theta_{py}, \theta_{pz}$  and  $\theta_{Fx}, \theta_{Fy}, \theta_{Fz}$ , which may depend on the grid size, time step and even velocity. It has been proven that some classical second-order projection methods [32,33] and SIMPLE-type methods [34,36] can be recovered from Eqs. (8)–(11) and Eqs. (12)–(15) with different coefficient matrices. The SIMPLE method has been shown to have second-order temporal accuracy for unsteady flows [37].

We can see the difference between the projection method I of Eqs. (8)–(11) and the projection method II of Eqs. (12)–(15). For the four-step projection method I, the pressure term always comes together with the Lorentz force. These two terms will be discretized at the same position. Both should be discretized at the same cell center point, or the same cell face center. While, in the projection method II, the Lorentz force is only calculated in the predictor step of Eq. (12). From Eqs. (13)–(15), the pressure term does not appear together with the Lorentz force.

The differences between the two projection methods can be understood based on a collocated grid system as shown in Fig. 1c. The Lorentz force is calculated based on  $\mathbf{J} \times \mathbf{B}$ . Using the projection method I, we need to calculate the Lorentz force not only at the cell center, but also at the cell faces, which requires interpolation of current density from one cell face to another in a control volume. The interpolation from face to face makes it hard to conserve current density, especially on an unstructured grid or a very non-uniform grid for high Hartmann numbers. The non-conservative interpolation of current density will introduce numerical errors for the calculation of Lorentz force on the cell faces. This numerical error makes that the balance between the pressure term and the Lorentz force in a fully developed core flow cannot be guaranteed.

For the projection method II, we only need to calculate the Lorentz force at the cell center in the first predictor step of Eq. (12). Using the collocated grid system of Fig. 1c, a conservative scheme will be designed to do the interpolation of current density from cell faces to cell center. This conservative interpolation can guarantee the balance between the pressure term and the Lorentz force at the cell center.

For the projection method I, one can get the pressure boundary condition as:

$$\left(\frac{\partial p_c^{k+1}}{\partial n}\right)_{BC} - N((\mathbf{J} \times \mathbf{B}) \cdot \mathbf{n})_{BC}^{k+1} = \left(\frac{\partial p_c^k}{\partial n}\right)_{BC} - N((\mathbf{J} \times \mathbf{B}) \cdot \mathbf{n})_{BC}^k \tag{16}$$

For the projection method II, the corresponding pressure boundary condition can be given as:

$$\left(\frac{\partial p_c^{k+1}}{\partial n}\right)_{BC} = \left(\frac{\partial p_c^k}{\partial n}\right)_{BC} \quad (17)$$

We can see that the simple Neumann condition works well for the projection method II, while the pressure boundary condition of Eq. (16) must take into account the Lorentz force on the boundary for the projection method I, especially for unsteady flows. Eq. (16) needs the current density along the tangential direction on the boundary faces, which add complexity for pressure boundary conditions.

We therefore prefer to the projection method II of Eqs. (12)–(15) for the simulation of incompressible Navier–Stokes equations couple with electromagnetic forces due to its simplicity of implementation and its accuracy of calculation for the Lorentz force.

### 2.3. Two three-step projection methods and boundary conditions for MHD flows

The above two four-step projection methods can also be reduced to the following three-step projection methods.

- Three-step projection method I (corresponding to the four-step projection method I of Eqs. (8)–(11)):

$$A\hat{u} = \mathbf{r}^k + \mathbf{G}p^k + N(\mathbf{J} \times \mathbf{B})^k \quad (18)$$

$$\Delta t \mathbf{D}(\Theta_p^k \mathbf{G}(p^{k+1} - p^k)) = \mathbf{D}(\hat{u} + \Delta t \Theta_F^k N((\mathbf{J} \times \mathbf{B})^{k+1} - (\mathbf{J} \times \mathbf{B})^k)) \quad (19)$$

$$\mathbf{u}^{k+1} = \hat{u} - \Delta t(\Theta_p^k \mathbf{G}(p^{k+1} - p^k) - \Theta_F^k N((\mathbf{J} \times \mathbf{B})^{k+1} - (\mathbf{J} \times \mathbf{B})^k)) \quad (20)$$

- Three-step projection method II (corresponding to the four-step projection method II of Eqs. (12)–(15)):

$$A\hat{u} = \mathbf{r}^k + \mathbf{G}p^k + N(\mathbf{J} \times \mathbf{B})^k \quad (21)$$

$$\Delta t \mathbf{D}(\Theta_p^k \mathbf{G}(p^{k+1} - p^k)) = \mathbf{D}(\hat{u}) \quad (22)$$

$$\mathbf{u}^{k+1} = \hat{u} - \Delta t \Theta_p^k \mathbf{G}(p^{k+1} - p^k) \quad (23)$$

The SIMPLE [34] and SIMPLEC [36] methods can be acquired from Eqs. (18)–(20) and Eqs. (21)–(23) with a non-linear coefficient matrix dependent on velocity, grid size and time step. The pressure boundary conditions for the three-step projection method I and three-step projection method II can be, respectively, given as:

$$\left(\frac{\partial(p_c^{k+1} - p_c^k)}{\partial n}\right)_{BC} = N(((\mathbf{J} \times \mathbf{B})^{k+1} - (\mathbf{J} \times \mathbf{B})^k) \cdot \mathbf{n})_{BC} \quad (24)$$

For the three-step projection method II, the corresponding pressure boundary conditions can be given as:

$$\left(\frac{\partial(p_c^{k+1} - p_c^k)}{\partial n}\right)_{BC} = 0 \quad (25)$$

Based on the same reasons for the choice of the four-step projection methods, we prefer to use the three-step projection method II for the calculation of MHD flows. In this paper, the calculation of MHD flows is performed using the four-step projection method II.

## 3. Consistent and conservative formula for current density and the Lorentz Force

### 3.1. Conservative laplace and divergence operators

On a collocated mesh, the calculation of the Lorentz force at the cell center is dependent on the current density. For a low magnetic Reynolds number, the current density can be calculated through Ohm's law [13–15]:

$$\mathbf{J} = -\nabla\varphi + \mathbf{u} \times \mathbf{B} \quad (26)$$

The current density includes two parts of  $\mathbf{J}_s = \nabla\varphi$ , the electrical potential gradient, and  $\mathbf{J}_u = \mathbf{u} \times \mathbf{B}$ , the Lorentz force dependent on velocity. Here the electrical potential is scaled with  $Lu_0B_0$ . Current density is conserved, and we must also enhance:

$$\nabla \cdot \mathbf{J} = 0 \tag{27}$$

From Eqs. (26) and (27), we can get the electrical potential Poisson equation as:

$$\nabla \cdot (\nabla\varphi) = \nabla \cdot (\mathbf{u} \times \mathbf{B}) \tag{28}$$

The discretization of the Laplace operator  $\nabla \cdot (\nabla)$  includes the discretization of the divergence operator and the gradient operator. The gradient operator is related to the calculation of current density. The discretization of the gradient operator in the Laplace operator in Eq. (28) should be consistent with the discretization of the gradient operator in the calculation of current density in Eq. (26). Also, the calculation of  $\mathbf{u} \times \mathbf{B}$  in the Poisson equation of Eq. (28) should be consistent with the calculation of  $\mathbf{J}_u$  for the current density at the cell face.

Integrating Eq. (27) over a control volume as shown in Fig. 1, we have:

$$\int_{\Omega} \nabla \cdot \mathbf{J} d\Omega = \oint_S \mathbf{n} \cdot \mathbf{J} ds = \sum_{f=1}^{nf} (\mathbf{n} \cdot \mathbf{J})_f s_f \tag{29}$$

The subscript  $f$  denotes the cell face, and  $nf$  is the total number of cell faces on the control volume, with  $nf = 4$  for two-dimensional rectangular and  $nf = 6$  for three-dimensional hexahedral cases, respectively. It is natural to locate the current density flux  $J_n = \mathbf{J} \cdot \mathbf{n}$  on the cell faces, which can effectively conserve the current density in the control volume. This arrangement is illustrated in the staggered grid system and collocated grid system in Fig. 1a and c.  $\varphi$  and  $p$  are located at the cell center and  $J_n$  is located at the cell face center, with  $J_x$  at  $(i + \frac{1}{2}, j, k)$ ,  $J_y$  at  $(i, j + \frac{1}{2}, k)$ , and  $J_z$  at  $(i, j, k + \frac{1}{2})$ . The velocities of  $u$ ,  $v$  and  $w$  are located at the cell center in the collocated grid system. In a finite volume grid, the cell center point is located at the center of a control volume.

The conservative discretized divergence operator for current density can be given for the controlled volume  $(i,j,k)$  as:

$$(\mathbf{D}_c(\mathbf{J}))_{i,j,k} = \frac{(J_x)_{i+\frac{1}{2},j,k} - (J_x)_{i-\frac{1}{2},j,k}}{x_{i+\frac{1}{2}} - x_{i-\frac{1}{2}}} + \frac{(J_y)_{i,j+\frac{1}{2},k} - (J_y)_{i,j-\frac{1}{2},k}}{y_{j+\frac{1}{2}} - y_{j-\frac{1}{2}}} + \frac{(J_z)_{i,j,k+\frac{1}{2}} - (J_z)_{i,j,k-\frac{1}{2}}}{z_{k+\frac{1}{2}} - z_{k-\frac{1}{2}}} \tag{30}$$

where  $\mathbf{J}_u$  is made up of  $\mathbf{J}_u$  and  $\mathbf{J}_s$ , we have:

$$(\mathbf{D}_c(\mathbf{J}_u))_{i,j,k} = \frac{(\mathbf{J}_u)_x)_{i+\frac{1}{2},j,k} - (\mathbf{J}_u)_x)_{i-\frac{1}{2},j,k}}{x_{i+\frac{1}{2}} - x_{i-\frac{1}{2}}} + \frac{(\mathbf{J}_u)_y)_{i,j+\frac{1}{2},k} - (\mathbf{J}_u)_y)_{i,j-\frac{1}{2},k}}{y_{j+\frac{1}{2}} - y_{j-\frac{1}{2}}} + \frac{(\mathbf{J}_u)_z)_{i,j,k+\frac{1}{2}} - (\mathbf{J}_u)_z)_{i,j,k-\frac{1}{2}}}{z_{k+\frac{1}{2}} - z_{k-\frac{1}{2}}} \tag{31}$$

$$(\mathbf{D}_c(\mathbf{J}_s))_{i,j,k} = \frac{(\mathbf{J}_s)_x)_{i+\frac{1}{2},j,k} - (\mathbf{J}_s)_x)_{i-\frac{1}{2},j,k}}{x_{i+\frac{1}{2}} - x_{i-\frac{1}{2}}} + \frac{(\mathbf{J}_s)_y)_{i,j+\frac{1}{2},k} - (\mathbf{J}_s)_y)_{i,j-\frac{1}{2},k}}{y_{j+\frac{1}{2}} - y_{j-\frac{1}{2}}} + \frac{(\mathbf{J}_s)_z)_{i,j,k+\frac{1}{2}} - (\mathbf{J}_s)_z)_{i,j,k-\frac{1}{2}}}{z_{k+\frac{1}{2}} - z_{k-\frac{1}{2}}} \tag{32}$$

$(J_x, J_y, J_z)$ ,  $(\mathbf{J}_u)_x, (\mathbf{J}_u)_y, (\mathbf{J}_u)_z$  and  $(\mathbf{J}_s)_x, (\mathbf{J}_s)_y, (\mathbf{J}_s)_z$  are three components of  $\mathbf{J}$ ,  $\mathbf{J}_u$  and  $\mathbf{J}_s$  in the  $x$ ,  $y$ , and  $z$  directions, respectively. Correspondingly, we have the following conservative discretized formulation of Eq. (28) at a controlled volume of:

$$\begin{aligned} (\mathbf{L}_c(\varphi))_{i,j,k} &= (\mathbf{D}_c(\mathbf{G}_f(\varphi)))_{i,j,k} \\ &= \frac{(\mathbf{G}_{fx}(\varphi))_{i+\frac{1}{2},j,k} - (\mathbf{G}_{fx}(\varphi))_{i-\frac{1}{2},j,k}}{x_{i+\frac{1}{2}} - x_{i-\frac{1}{2}}} + \frac{(\mathbf{G}_{fy}(\varphi))_{i,j+\frac{1}{2},k} - (\mathbf{G}_{fy}(\varphi))_{i,j-\frac{1}{2},k}}{y_{j+\frac{1}{2}} - y_{j-\frac{1}{2}}} + \frac{(\mathbf{G}_{fz}(\varphi))_{i,j,k+\frac{1}{2}} - ((\mathbf{G}_{fz}(\varphi))_{i,j,k-\frac{1}{2}})}{z_{k+\frac{1}{2}} - z_{k-\frac{1}{2}}} \\ &= (\mathbf{D}_c((\mathbf{J}_u)_f))_{i,j,k} \end{aligned} \tag{33}$$

Here  $\mathbf{D}_c$  is a discretized divergence operator,  $\mathbf{L}_c$  is a discretized Laplace operator at the cell center, and  $\mathbf{G}_f$  is a gradient operator discretized at the cell face.  $\mathbf{G}_{fx}$ ,  $\mathbf{G}_{fy}$ ,  $\mathbf{G}_{fz}$  are the projectors of  $\mathbf{G}_f$  in the  $x$ ,  $y$ ,  $z$  directions, respectively. The subscript  $c$  denotes the cell center, and  $f$  denotes the cell face.

### 3.2. Consistent gradient operator and interpolation operator at cell face to ensure calculated current flux conservative

Since the conservative discretized divergence and Laplace operators of Eqs. (30) and (33) need the value of current density on the cell faces, we now give the discretized gradient operator of electrical potential and interpolation operator for velocity on the cell faces. The gradient operator can be given as:

$$(Js_x)_{i+\frac{1}{2},j,k} = -(\mathbf{G}_{fx}(\varphi))_{i+\frac{1}{2},j,k} = -\frac{\varphi_{i+1,j,k} - \varphi_{i,j,k}}{x_{i+1} - x_i} \quad (34)$$

$$(Js_y)_{i,j+\frac{1}{2},k} = -(\mathbf{G}_{fy}(\varphi))_{i,j+\frac{1}{2},k} = -\frac{\varphi_{i,j+1,k} - \varphi_{i,j,k}}{y_{j+1} - y_j} \quad (35)$$

$$(Js_z)_{i,j,k+\frac{1}{2}} = -(\mathbf{G}_{fz}(\varphi))_{i,j,k+\frac{1}{2}} = -\frac{\varphi_{i,j,k+1} - \varphi_{i,j,k}}{z_{k+1} - z_k} \quad (36)$$

This discretized gradient operator in the calculation of current density has been forced to be consistent with the corresponding part in the calculation of Laplace operator. In other words, Eqs. (34)–(36) are consistent with Eq. (33). In the discretized divergence operator on  $\mathbf{J}\mathbf{u}$  from Eq. (31), the detailed formula can be given as:

$$(\mathbf{J}u_x)_{i+\frac{1}{2},j,k} = v_{i+\frac{1}{2},j,k}(B_z)_{i+\frac{1}{2},j,k} - w_{i+\frac{1}{2},j,k}(B_y)_{i+\frac{1}{2},j,k} \quad (37)$$

$$(\mathbf{J}u_y)_{i,j+\frac{1}{2},k} = w_{i,j+\frac{1}{2},k}(B_x)_{i,j+\frac{1}{2},k} - u_{i,j+\frac{1}{2},k}(B_z)_{i,j+\frac{1}{2},k} \quad (38)$$

$$(\mathbf{J}u_z)_{i,j,k+\frac{1}{2}} = u_{i,j,k+\frac{1}{2}}(B_y)_{i,j,k+\frac{1}{2}} - v_{i,j,k+\frac{1}{2}}(B_x)_{i,j,k+\frac{1}{2}} \quad (39)$$

where  $\mathbf{B}$  is assumed known. The calculation of  $\mathbf{J}\mathbf{u}$  is dependent on the velocity, which is related to grid arrangement. On a collocated grid system, an interpolation operator of  $\Lambda_{c \rightarrow f}$  can be defined, which represents the interpolation from cell center to cell face since  $u, v, w$  are located at the cell center for a collocated grid system:

$$\mathbf{V}_f = \Lambda_{c \rightarrow f}(\mathbf{V}_c) \quad (40)$$

Let  $\mathbf{u}$  denote the velocity vector of  $(u, v, w)$ , and we have a detailed formula of the interpolation operator on collocated grids:

$$\mathbf{u}_{i+\frac{1}{2},j,k} = \Lambda_{c \rightarrow fx+}(\mathbf{u}_c) = \alpha_+ \mathbf{u}_{i,j,k} + (1 - \alpha_+) \mathbf{u}_{i+1,j,k} \quad (41)$$

$$\mathbf{u}_{i,j+\frac{1}{2},k} = \Lambda_{c \rightarrow fy+}(\mathbf{u}_c) = \beta_+ \mathbf{u}_{i,j,k} + (1 - \beta_+) \mathbf{u}_{i,j+1,k} \quad (42)$$

$$\mathbf{u}_{i,j,k+\frac{1}{2}} = \Lambda_{c \rightarrow fz+}(\mathbf{u}_c) = \gamma_+ \mathbf{u}_{i,j,k} + (1 - \gamma_+) \mathbf{u}_{i,j,k+1} \quad (43)$$

The subscripts  $c \rightarrow fx+$ ,  $c \rightarrow fy+$ , and  $c \rightarrow fz+$  denote the interpolation from cell center to cell faces normal to the  $x$ -,  $y$ - and  $z$ -directions, respectively. The symbol  $+$  denotes that the cell faces are located to the right, top and front of the cell center, respectively. Now, we can give the detailed formula for the interpolation operator from cell center to cell face center as:

$$(\mathbf{V}_{f+})_{i,j,k} = \begin{pmatrix} \mathbf{u}_{i+\frac{1}{2},j,k} \\ \mathbf{u}_{i,j+\frac{1}{2},k} \\ \mathbf{u}_{i,j,k+\frac{1}{2}} \end{pmatrix} = \begin{pmatrix} \Lambda_{c \rightarrow fx+}(\mathbf{u}) \\ \Lambda_{c \rightarrow fy+}(\mathbf{u}) \\ \Lambda_{c \rightarrow fz+}(\mathbf{u}) \end{pmatrix}_{i,j,k} = \Lambda_{c \rightarrow f+}(\mathbf{V}_c)_{i,j,k} \quad (44)$$

In a similar way, we can get:

$$(\mathbf{V}_{f-})_{i,j,k} = \begin{pmatrix} \mathbf{u}_{i-\frac{1}{2},j,k} \\ \mathbf{u}_{i,j-\frac{1}{2},k} \\ \mathbf{u}_{i,j,k-\frac{1}{2}} \end{pmatrix} = \begin{pmatrix} \Lambda_{c \rightarrow fx-}(\mathbf{u}) \\ \Lambda_{c \rightarrow fy-}(\mathbf{u}) \\ \Lambda_{c \rightarrow fz-}(\mathbf{u}) \end{pmatrix}_{i,j,k} = \Lambda_{c \rightarrow f-}(\mathbf{V}_c)_{i,j,k} \quad (45)$$

Here the symbol  $-$  denotes that the cell faces are located to the left, bottom and back of a cell center in a controlled volume. Omitting the subscript  $(i, j, k)$  in Eqs. (44) and (45), we therefore have the general interpolation formula of Eq. (40) from cell center to cell face.

In Eqs. (41)–(43), the interpolation has second-order accuracy if we have:

$$\alpha_+ = \frac{x_{i+1} - x_{i+\frac{1}{2}}}{x_{i+1} - x_i}, \quad \beta_+ = \frac{y_{j+1} - y_{j+\frac{1}{2}}}{y_{j+1} - y_j}, \quad \gamma_+ = \frac{z_{k+1} - z_{k+\frac{1}{2}}}{z_{k+1} - z_k} \quad (46)$$

However, this interpolation is not symmetrical between neighbor points of a cell face, while the discretization of the gradient operator at the cell face is symmetrical. To keep consistency between the calculations for  $\mathbf{J}_s$  and  $\mathbf{J}_u$ , we can choose:

$$\alpha_+ = \frac{1}{2}, \quad \beta_+ = \frac{1}{2}, \quad \gamma_+ = \frac{1}{2} \quad (47)$$

Now we give a brief summary of Sections 3.1 and 3.2. Eqs. (30) and (33) give a conservative discretized formula for the divergence and the Laplace operators. By solving the conservative discretized electrical potential equation of Eq. (33), and calculating the interface current density of  $\mathbf{J}_{s_f}$  based on Eqs. (34)–(36) and of  $\mathbf{J}_{u_f}$  from Eqs. (37)–(39), with velocity interpolation operator of Eq. (40) and the average coefficient of Eq. (47) employed, the current density should be conserved in a control volume. The calculation of  $\mathbf{J}_{u_f}$  on the cell face based on Eqs. (37)–(39) with the velocity interpolation formula of Eqs. (40) and (47) for a collocated grid system are consistent with the discretized formula for  $\mathbf{J}_{s_f}$  on the cell face using Eqs. (34)–(36). Both the interpolation operator of Eq. (40) and gradient operator of Eqs. (34)–(36) are consistent with the discretization of the divergence operator of Eqs. (31) and (32) and the Laplace operator of Eq. (33), and therefore they are also conservative and consistent.

### 3.3. Calculation of the Lorentz force at cell center

#### 3.3.1. Conservative formula

The calculation of the Lorentz force in the momentum equations (3) and (12) can be described as:

$$\mathbf{F} = (\mathbf{J} \times \mathbf{B}) = (-\nabla\phi + \mathbf{u} \times \mathbf{B}) \times \mathbf{B} \quad (48)$$

On a collocated grid system, we have the Lorentz force at a cell center as:

$$(F_x)_{i,j,k} = (J_y B_z - J_z B_y)_{i,j,k} = (J_y)_{i,j,k} (B_z)_{i,j,k} - (J_z)_{i,j,k} (B_y)_{i,j,k} \quad (49)$$

$$(F_y)_{i,j,k} = (J_z B_x - J_x B_z)_{i,j,k} = (J_z)_{i,j,k} (B_x)_{i,j,k} - (J_x)_{i,j,k} (B_z)_{i,j,k} \quad (50)$$

$$(F_z)_{i,j,k} = (J_x B_y - J_y B_x)_{i,j,k} = (J_x)_{i,j,k} (B_y)_{i,j,k} - (J_y)_{i,j,k} (B_x)_{i,j,k} \quad (51)$$

We calculate the current density fluxes on the cell faces of the control finite volume from the consistent and conservative discretized operators developed in Section 3.2. Since the current density fluxes  $J_x$ ,  $J_y$  and  $J_z$  are located on the cell faces normal to the  $x$ -,  $y$ - and  $z$ -directions, respectively, interpolation from cell faces to cell center is needed to calculate the Lorentz force at the cell center. We now define a conservative interpolation operator  $\mathbf{\Lambda}_{f \rightarrow c}$ , which represents interpolation from cell face to cell center:

$$\mathbf{J}_c = \mathbf{\Lambda}_{f \rightarrow c}(\mathbf{J}_f) \quad (52)$$

The detailed formula can be given on a control volume as:

$$(J_x)_{i,j,k} = (\mathbf{\Lambda}_{f_x \rightarrow c}((J_x)_{f_x}))_{i,j,k} = \frac{1}{2}((J_x)_{i+\frac{1}{2},j,k} + (J_x)_{i-\frac{1}{2},j,k}) \quad (53)$$

$$(J_y)_{i,j,k} = (\mathbf{\Lambda}_{f_y \rightarrow c}((J_y)_{f_y}))_{i,j,k} = \frac{1}{2}((J_y)_{i,j+\frac{1}{2},k} + (J_y)_{i,j-\frac{1}{2},k}) \quad (54)$$

$$(J_z)_{i,j,k} = (\mathbf{\Lambda}_{f_z \rightarrow c}((J_z)_{f_z}))_{i,j,k} = \frac{1}{2}((J_z)_{i,j,k+\frac{1}{2}} + (J_z)_{i,j,k-\frac{1}{2}}) \quad (55)$$

Eqs. (53)–(55) can be written as a vector formula:

$$(\mathbf{J}_c)_{i,j,k} = \begin{pmatrix} (\mathbf{J}_x)_c \\ (\mathbf{J}_y)_c \\ (\mathbf{J}_z)_c \end{pmatrix}_{i,j,k} = \begin{pmatrix} \Lambda_{fx \rightarrow c}((\mathbf{J}_x)_{fx}) \\ \Lambda_{fy \rightarrow c}((\mathbf{J}_y)_{fy}) \\ \Lambda_{fz \rightarrow c}((\mathbf{J}_z)_{fz}) \end{pmatrix}_{i,j,k} = (\Lambda_{f \rightarrow c}(\mathbf{J}_f))_{i,j,k} \quad (56)$$

Omitting the subscript  $(i, j, k)$  in Eq. (56), we therefore have the general interpolation formula of Eq. (52) from cell faces to cell center. The interpolation is based on the conservative current density fluxes on the cell faces. The interpolation procedure of Eq. (56) meets the conservation condition of  $\mathbf{J} = \nabla \cdot (\mathbf{J}\mathbf{r})$  ( $\mathbf{r}$  denotes the distance vector), which will be detailed discussed in our next paper [30] for the construction of consistent and conservative scheme on an unstructured grid system [30]. The calculation of the Lorentz force using Eqs. (49)–(51) together with Eq. (52) or Eq. (56) will be consistent and conservative, which can conserve the total momentum as proven in [30]. Therefore this scheme is conservative and consistent.

### 3.3.2. A non-conservative formula

Since  $\mathbf{J} = \mathbf{J}_u + \mathbf{J}_s$ , the calculation of the Lorentz force of Eq. (48) can be decomposed into two parts, which are:

$$\mathbf{J}_s \times \mathbf{B} = -\nabla \phi \times \mathbf{B} \quad (57)$$

$$\mathbf{J}_u \times \mathbf{B} = (\mathbf{u} \times \mathbf{B}) \times \mathbf{B} \quad (58)$$

$\mathbf{J}_s$  and  $\mathbf{J}_u$  can be interpolated, respectively as:

$$(\mathbf{J}_s)_c)_{i,j,k} = \begin{pmatrix} (\mathbf{J}_{s_x})_c \\ (\mathbf{J}_{s_y})_c \\ (\mathbf{J}_{s_z})_c \end{pmatrix}_{i,j,k} = \begin{pmatrix} \Lambda_{fx \rightarrow c}((\mathbf{J}_{s_x})_{fx}) \\ \Lambda_{fy \rightarrow c}((\mathbf{J}_{s_y})_{fy}) \\ \Lambda_{fz \rightarrow c}((\mathbf{J}_{s_z})_{fz}) \end{pmatrix}_{i,j,k} = (\Lambda_{f \rightarrow c}(\mathbf{J}_s))_{i,j,k} \quad (59)$$

$$(\mathbf{J}_u)_c)_{i,j,k} = \begin{pmatrix} (\mathbf{J}_{u_x})_c \\ (\mathbf{J}_{u_y})_c \\ (\mathbf{J}_{u_z})_c \end{pmatrix}_{i,j,k} = \begin{pmatrix} \Lambda_{fx \rightarrow c}((\mathbf{J}_{u_x})_{fx}) \\ \Lambda_{fy \rightarrow c}((\mathbf{J}_{u_y})_{fy}) \\ \Lambda_{fz \rightarrow c}((\mathbf{J}_{u_z})_{fz}) \end{pmatrix}_{i,j,k} = (\Lambda_{f \rightarrow c}(\mathbf{J}_u))_{i,j,k} \quad (60)$$

Eq. (59) for the calculation of  $\mathbf{J}_{s_c}$ , together with Eq. (60) for  $\mathbf{J}_{u_c}$  will form the conservative and consistent scheme of Eq. (56) developed in the above section. However,  $\mathbf{J}_{s_c}$  can also be calculated directly from the electrical potential gradient as follows:

$$(\mathbf{J}_{s_x})_{i,j,k} = -((\mathbf{G}_c \phi)_x)_{i,j,k} = \frac{\phi_{i+1,j,k} - \phi_{i-1,j,k}}{x_{i+1} - x_{i-1}} \quad (61)$$

$$(\mathbf{J}_{s_y})_{i,j,k} = -((\mathbf{G}_c \phi)_y)_{i,j,k} = \frac{\phi_{i,j+1,k} - \phi_{i,j-1,k}}{y_{j+1} - y_{j-1}} \quad (62)$$

$$(\mathbf{J}_{s_z})_{i,j,k} = -((\mathbf{G}_c \phi)_z)_{i,j,k} = \frac{\phi_{i,j,k+1} - \phi_{i,j,k-1}}{z_{k+1} - z_{k-1}} \quad (63)$$

Eqs. (61)–(63) can be written in a vector formula as:

$$(\mathbf{J}_s)_c)_{i,j,k} = \begin{pmatrix} (\mathbf{J}_{s_x})_c \\ (\mathbf{J}_{s_y})_c \\ (\mathbf{J}_{s_z})_c \end{pmatrix}_{i,j,k} = - \begin{pmatrix} (\mathbf{G}_c \phi)_x \\ (\mathbf{G}_c \phi)_y \\ (\mathbf{G}_c \phi)_z \end{pmatrix}_{i,j,k} = -(\mathbf{G}_c \phi)_{i,j,k} \quad (64)$$

Omitting the subscript  $(i, j, k)$  in Eq. (64), we therefore have

$$\mathbf{J}_{s_c} = -\mathbf{G}_c \phi \quad (65)$$

Eqs. (64) and (65) are not conservative on a non-uniform grid system for high Hartmann cases. Eq. (64) is consistent with Eq. (59) on a uniform grid system; however, they are not consistent on any non-uniform grid

system. Eqs. (64) and (65) are not consistent with the discretized Laplacian operator of Eq. (33). Indeed, the conservative and consistent scheme of Eq. (59) can be given as:

$$(Js_x)_{i,j,k} = \frac{1}{2} \left( \frac{\varphi_{i+1,j,k} - \varphi_{i,j,k}}{x_{i+1} - x_i} + \frac{\varphi_{i,j,k} - \varphi_{i-1,j,k}}{x_i - x_{i-1}} \right) \tag{66}$$

$$(Js_y)_{i,j,k} = \frac{1}{2} \left( \frac{\varphi_{i,j+1,k} - \varphi_{i,j,k}}{y_{j+1} - y_j} + \frac{\varphi_{i,j,k} - \varphi_{i,j-1,k}}{y_j - y_{j-1}} \right) \tag{67}$$

$$(Js_z)_{i,j,k} = \frac{1}{2} \left( \frac{\varphi_{i,j,k+1} - \varphi_{i,j,k}}{z_{k+1} - z_k} + \frac{\varphi_{i,j,k} - \varphi_{i,j,k-1}}{z_k - z_{k-1}} \right) \tag{68}$$

We now analyze the schemes of Eqs. (61)–(63) and Eqs. (66)–(68). As we already mentioned in the introduction, the calculation of Eqs. (61)–(63) should be same as the formula of Eqs. (66)–(68) on a uniform grid system. They both are conservative for low Hartmann number cases with uniform grid systems employed. However, Eqs. (66)–(68) are very different with Eqs. (61)–(63) on a non-uniform grid system. Eqs. (66)–(68) are conservative interpolation formulae based on conservative current density fluxes on cell faces, while (61)–(63) are not based on the conservative formulae. Without loss of generality, Eqs. (63) and (68) are used to conduct the analysis. With the subscripts  $i,j$  omitted, we now analyze the following two equations:

$$\left( \frac{\partial \varphi}{\partial z} \right)_k = \frac{\varphi_{k+1} - \varphi_{k-1}}{z_{k+1} - z_{k-1}} \tag{69}$$

$$\left( \frac{\partial \varphi}{\partial z} \right)_k = \frac{1}{2} \left( \frac{\varphi_{k+1} - \varphi_k}{z_{k+1} - z_k} + \frac{\varphi_k - \varphi_{k-1}}{z_k - z_{k-1}} \right) \tag{70}$$

Using the Taylor series, it is not difficult to get the modified equations of Eqs. (69) and (70), respectively as:

$$\frac{\varphi_{k+1} - \varphi_{k-1}}{z_{k+1} - z_{k-1}} = \frac{\partial \varphi}{\partial z} + \frac{1}{2} \frac{\partial^2 \varphi}{\partial z^2} (z_{k+1} - 2z_k + z_{k-1}) + \frac{1}{6} \frac{\partial^3 \varphi}{\partial z^3} f(z) + \dots \tag{71}$$

$$\frac{1}{2} \left( \frac{\varphi_{k+1} - \varphi_k}{z_{k+1} - z_k} + \frac{\varphi_k - \varphi_{k-1}}{z_k - z_{k-1}} \right) = \frac{\partial \varphi}{\partial z} + \frac{1}{4} \frac{\partial^2 \varphi}{\partial z^2} (z_{k+1} - 2z_k + z_{k-1}) + \frac{1}{12} \frac{\partial^3 \varphi}{\partial z^3} g(z) + \dots \tag{72}$$

With  $g(z) = (z_{k+1} - z_{k-1})(z_{k+1} - 2z_k + z_{k-1})$ , and  $f(z) = (z_{k+1} - z_{k-1})^{-1}(z_{k+1} - 2z_k + z_{k-1})((z_{k+1} - z_k)^2 + (z_k - z_{k-1}) + (z_k - z_{k-1})^2)$  we can prove that  $f(z) \geq \frac{1}{2}g(z)$ . From the modified equations (71) and (72), we can see that the leading error term of Eq. (71) is double the leading error term of Eq. (72), and the second error term of Eq. (71) is also greater than the corresponding error term of Eq. (72). These increased error terms in Eq. (71) make the scheme of Eqs. (61)–(63) neither conservative nor consistent, while the scheme of Eqs. (66)–(68) is both conservative and consistent. These increased error terms cannot get a good result for high Hartmann number cases of MHD using the inconsistent scheme.

The second part of the Lorentz force in Eq. (58) can be written as:

$$\mathbf{J} \mathbf{u} \times \mathbf{B} = (\mathbf{u} \times \mathbf{B}) \times \mathbf{B} = \mathbf{B}^2 \mathbf{u}_\perp \tag{73}$$

This part of the Lorentz force is corresponding to the velocity itself. On a collocated grid system, the velocity at the center point itself can be directly used as the second part of the Lorentz force, and we then have:

$$(\mathbf{J} \mathbf{u} \times \mathbf{B})_c = \mathbf{B}_c^2 (\mathbf{u}_c)_\perp \tag{74}$$

However, the conservative discretized divergence operator of  $\mathbf{J} \mathbf{u}$  is based on the velocity at the cell face. Eq. (74) is not based on conservative current density, and it is not consistent with the discretized divergence operator of Eq. (30) and the Laplace operator of Eq. (33). There is one choice to keep this portion of Lorentz force calculated based on a conservative formula as:

$$(\mathbf{u}_c)_{i,j,k} = \begin{pmatrix} u \\ v \\ w \end{pmatrix}_{i,j,k} = \begin{pmatrix} \Lambda_{fx \rightarrow c}(u) \\ \Lambda_{fy \rightarrow c}(v) \\ \Lambda_{fz \rightarrow c}(w) \end{pmatrix}_{i,j,k} = (\Lambda_{f \rightarrow c}(\mathbf{u}_f))_{i,j,k} \tag{75}$$

Omitting the subscript  $(i,j,k)$ , Eq. (75) can be given as:

$$\mathbf{u}_c = \Lambda_{f \rightarrow c}(\mathbf{u}_f) \tag{76}$$

Eq. (76) can be used to perform the calculation of  $\mathbf{u}_\perp$  at the cell center.

3.3.3. Testing schemes for the calculation of the Lorentz force in this paper

To test the effects of schemes on the calculated results for MHD at high Hartmann number cases, we now give the following four schemes for the calculation of the Lorentz force at the cell center:

- Scheme I
  - (1) Calculate  $\mathbf{J}_f$  on the cell faces using consistent schemes of Eqs. (34)–(36) for  $\mathbf{J}_{s_f}$  and Eqs. (37)–(40) and (47) for  $\mathbf{J}_{u_f}$ ;
  - (2) Calculate the Lorentz force at cell center using Eq. (48) or Eqs. (49)–(51). The current density of  $\mathbf{J}_c$  at the cell center used to calculate the Lorentz force is acquired from a conservative interpolation of Eq. (52) based on  $\mathbf{J}_f$  from step (1). This step is equivalent to using Eq. (59) for the calculation of  $\mathbf{J}_{s_c}$ , which is used to calculate the first part of the Lorentz force using Eq. (57) at a cell center, while the second part of the Lorentz force is calculated using Eq. (73) with velocity acquired from Eq. (75) or Eq. (76).

Fig. 3a illustrates the grid arrangement for current density of  $J_x$  and  $J_y$  of Scheme I.

- Scheme II
  - (1) Use inconsistent scheme of Eqs. (61)–(63) for the calculation of  $\mathbf{J}_{s_c}$ , which is used to calculate the first part of the Lorentz force using Eq. (57);
  - (2) Calculate the second part of the Lorentz force from Eq. (74), based on the velocity at the cell center directly.

Fig. 3b shows the grid arrangement for current density of  $J_x$  and  $J_y$  of Scheme II.

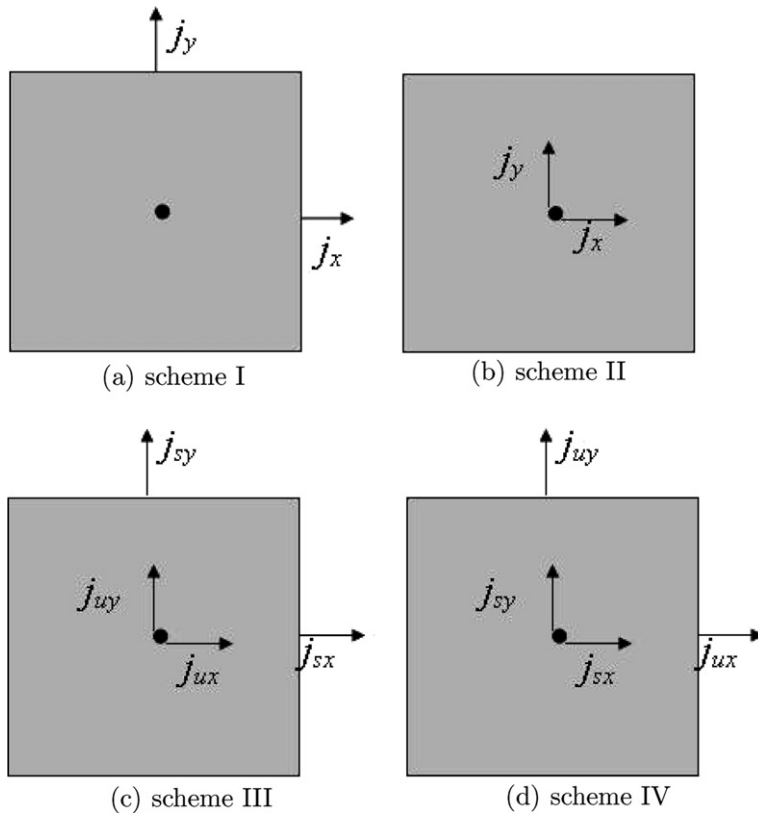


Fig. 3. Four schemes for calculations of the current density and the Lorentz force.

• Scheme III

- (1) Calculate  $\mathbf{J}_f$  from the consistent formula of Eqs. (34)–(36);
- (2) Calculate  $\mathbf{J}_c$  from the conservative interpolation scheme of Eq. (59), which is used to calculate first part of the Lorentz force from Eq. (57) at a cell center;
- (3) Calculate the second part of the Lorentz force from Eq. (74), based on the velocity at the cell center directly.

Fig. 3c shows the grid arrangement for current density of  $J_x$  and  $J_y$  of Scheme III.

• Scheme IV

- (1) Use the inconsistent and non-conservative scheme of Eqs. (61)–(63) for the calculation of  $\mathbf{J}_c$  which is used to calculate the first part of the Lorentz force using Eq. (57);
- (2) Use the conservative interpolation of Eq. (76) to get the velocity at the cell center, which is used to get the second part of the Lorentz force based on Eq. (74).

Fig. 3d shows the grid arrangement for current density of  $J_x$  and  $J_y$  of Scheme IV.

Scheme I is a consistent and conservative formula. The Lorentz force is acquired based on the conservative current density. In Scheme II, both  $\mathbf{J}_c$  and  $\mathbf{J}_f$  are not based on conservative current density on the cell face. It is a non-conservative and inconsistent formula. In Scheme III, the acquisition of  $\mathbf{J}_c$  is based on a conservative formula, however  $\mathbf{J}_f$  is not. In Scheme IV, the acquisition of  $\mathbf{J}_c$  is not based on a conservative formula, however  $\mathbf{J}_f$  is.

### 3.4. Consistent and conservative methods on a collocated grid system

We now summarize the schemes developed in the above subsections, and give a detailed computation procedure for MHD flows using consistent and conservative schemes for the current density on a collocated grid system. The four-step projection method of Eqs. (12)–(15) is applied on a collocated mesh, which can be written as:

$$\mathbf{A}_c \hat{\mathbf{u}}_c = \mathbf{r}_c^k + \mathbf{G}_c(p_c^k) + N(\mathbf{J} \times \mathbf{B})_c^k \tag{77}$$

$$\tilde{\mathbf{u}}_c = \hat{\mathbf{u}}_c + \Delta t \Theta_c^k \mathbf{G}_c(p_c^k) \tag{78}$$

$$\Delta t \mathbf{D}_c(\Theta_f^k \mathbf{G}_f(p_c^{k+1})) = \mathbf{D}_c(\Lambda_{c \rightarrow f}(\tilde{\mathbf{u}}_c)) \tag{79}$$

$$\mathbf{u}_c^{k+1} = \tilde{\mathbf{u}}_c - \Delta t \Theta_c^k \mathbf{G}_c(p_c^{k+1}) \tag{80}$$

$$\mathbf{u}_f^{k+1} = \Lambda_{c \rightarrow f}(\tilde{\mathbf{u}}_c) - \Delta t \Theta_f^k \mathbf{G}_f(p_c^{k+1}) \tag{81}$$

$$(\mathbf{u} \times \mathbf{B})_f^{k+1} = \Lambda_{c \rightarrow f}(\tilde{\mathbf{u}}_c^{k+1}) \times \mathbf{B}_f^{k+1} \tag{82}$$

$$\mathbf{D}_c(\mathbf{G}_f(\varphi_c^{k+1})) = \mathbf{D}_c((\mathbf{u} \times \mathbf{B})_f^{k+1}) \tag{83}$$

$$(J_n)_f^{k+1} = -(\mathbf{G}_f(\varphi_c^{k+1})) \cdot \mathbf{n}_f + (\mathbf{u} \times \mathbf{B})_f^{k+1} \cdot \mathbf{n}_f \tag{84}$$

$$(\mathbf{J} \times \mathbf{B})_c^{k+1} = \Lambda_{f \rightarrow c}((J_n)_f^{k+1}) \times \mathbf{B}_f^{k+1} \tag{85}$$

The complete algorithm from time step  $k$  to time step  $k + 1$  based on the four-step projection method II can be summarized as:

- (1) Evaluate Lorentz force  $(\mathbf{J} \times \mathbf{B})_c^k$  at time level  $k$ ; Calculate  $\mathbf{G}_c(p_c^k)$ ;
- (2) Evaluate coefficient matrices  $\Theta_c^k, \Theta_f^k$ ;
- (3) Solve the predictor step of Eq. (77) for  $\hat{\mathbf{u}}_c$ ; obtain the second intermediate velocity  $\tilde{\mathbf{u}}_c$  using Eq. (78); transfer the cell center velocity  $\tilde{\mathbf{u}}_c$  to face center velocity  $\tilde{\mathbf{u}}_f$  using  $\tilde{\mathbf{u}}_f = \Lambda_{c \rightarrow f}(\tilde{\mathbf{u}}_c)$ ;
- (4) Solve the pressure Poisson equation of Eq. (79) for  $p_c^{k+1}$ ; calculate  $\mathbf{G}_c(p_c^{k+1})$  and  $\mathbf{G}_f(p_c^{k+1})$ ;
- (5) Correct the velocity  $\mathbf{u}_c^{k+1}$  at cell center based on  $\tilde{\mathbf{u}}_c$ , and  $\mathbf{G}_c(p_c^{k+1})$  using Eq. (80); correct the velocity  $\mathbf{u}_f^{k+1}$  at face center based on  $\tilde{\mathbf{u}}_f$  and  $\mathbf{G}_f(p_c^{k+1})$ ;
- (6) Calculate  $(\mathbf{u} \times \mathbf{B})_f^{k+1}$  using Eq. (82); solve the electrical potential equation for  $\varphi_c^{k+1}$ ;

- (7) Calculate  $\mathbf{G}_f(\varphi_c^{k+1})$  and calculate the current density flux of  $(J_n)_f^{k+1}$  at the cell face using Eq. (84);
- (8) Calculate the Lorentz force of  $(\mathbf{J} \times \mathbf{B})_c^{k+1}$  at the cell center based on a conservative formula of Eq. (85);
- (9) Repeat Steps 2 through 8 for next time level.

The above projection method can balance the pressure term and the Lorentz force in the fully developed core flow. The consistent and conservative scheme developed in this paper is used to calculate the Lorentz force at the cell center. This includes the calculation of current density fluxes at the cell faces using a consistent and conservative scheme, and the current density at the cell center conservatively interpolated from the cell faces to cell center. We will validate our methods in the next section.

#### 4. Validation and application of consistent and conservative schemes

There exist some exact solutions for fully developed incompressible laminar flows in ducts with transverse magnetic fields, such as: (1) Shercliff's solution for rectangular ducts with non-conducting walls and the field perpendicular to one side [7]; (2) Hunt's solution for rectangular ducts with two non-conductive side walls (parallel to the field) and two conductive Hartmann walls (normal to the field) [8]. These two solutions will be used in this paper to verify our methods developed above.

##### 4.1. Shercliff's case

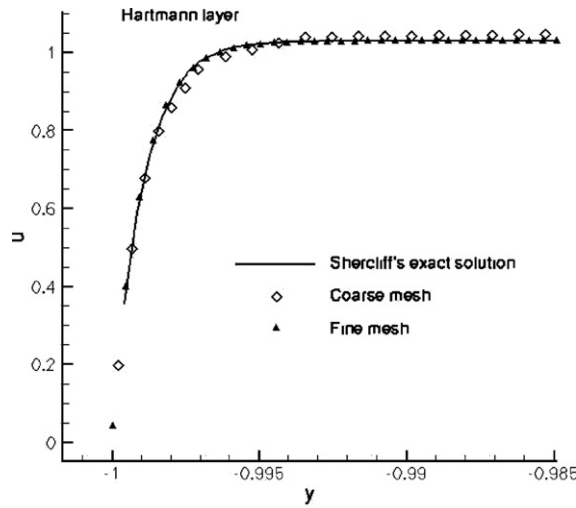
We simulate Shercliff's case with all of the walls electrically insulated. We present some preliminary results from a fully developed flow calculation at  $Ha = 1000$  and  $Re = 10$ , a mass flow rate of 4 and a pressure gradient from Shercliff's solution (with appropriate numerical implementation) of  $-102.88$ . Velocity distributions calculated on non-uniform meshes using the consistent and conservative scheme (Scheme I) are shown in Fig. 4. We present a comparison between the exact solution from Shercliff's analysis compared with the coarse and fine mesh solutions in Fig. 4. As can be seen the comparison is better than 0.1% for the fine mesh case with  $66 \times 66$  non-uniform grids employed. The solution on the coarse mesh with  $33 \times 33$  non-uniform grids indicates an error of about 0.5% in mass flow rate and peak velocity with uniform convergence. This figure illustrates the comparison in the Hartmann layer and side layers using Scheme I. The results from coarse grid and fine grids match the analytical results well. The comparison demonstrates a very good computational accuracy.

##### 4.1.1. Conservation

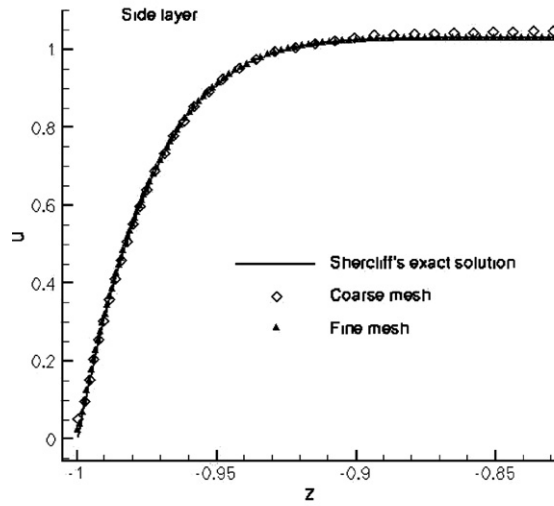
Now we analyze the difference between different schemes. Fig. 5 illustrates the iteration history of the flow rate using the above mentioned four schemes on  $33 \times 33$  and  $66 \times 66$  non-uniform grids, respectively. Both Fig. 5a and b show that consistent and conservative Scheme I can give an accurate result of flow rate, while the other non-conservative and inconsistent schemes cannot give accurate results. Schemes II and III give a lower flow rate, with the lowest value from Scheme III, while Scheme IV gives a higher value.

Fig. 6 shows the comparison between Shercliff's analytical results and numerical results from a  $66 \times 66$  non-uniform mesh. From this figure, we can see the velocity from Scheme I matches the analytical result pretty well, while Scheme II and Scheme III get lower velocities compared to the Shercliff's analytical result. Scheme IV can give good results in the core flow; however, in the side layers, there is an unphysical velocity jump.

Fig. 7 illustrates the iteration history of the divergence of current density on a  $66 \times 66$  grid. Fig. 7a is the history of the maximum value of the divergence. In Scheme I, the current density fluxes at the cell faces are calculated using a consistent method, which are used to get the divergence of current at a center of a control volume. In Scheme II, the current density fluxes at the cell faces, which are needed for the calculation of divergence, are interpolated from the current density calculated at the cell center. In Scheme III, the current density fluxes related to the electrical potential are calculated at the cell faces using a consistent method, while the velocity relevant parts are calculated by interpolating from cell center to cell face. In Scheme IV, the current fluxes related to the electrical potential are interpolated from the calculated value at the cell center. Generally, the current density fluxes on the cell faces from Scheme II and Scheme IV are not calculated from a consistent scheme with the electrical potential equation, while the methods of Scheme I and Scheme III for current



(a) Hartmann layer



(b) side layer

Fig. 4. A comparison of numerical and exact solutions at  $Ha = 1000$ .

density flux at the cell faces are consistent. From Fig. 7a, we can see that the divergences of current go to a very small value as iteration marches for the consistent Scheme I and Scheme III. However, the divergences of current are large and constant as iteration marches for the inconsistent Scheme II and Scheme IV. The history of  $L_2$  error of divergence of current density (see Fig. 7b) tells the similar story. These figures show us that consistent Scheme I and Scheme III can conserve the current density in a control volume, while Scheme II and Scheme IV cannot conserve the current density. The non-conservative Schemes II and IV cannot give the correct results.

Fig. 8 gives the distribution of current density at cell centers from results on a coarse mesh with  $33 \times 33$  non-uniform grids. This current density at cell centers will be used to calculate the Lorentz force. The current density from Scheme I (Fig. 8a) traces a closed streamline, which means the current density used to calculate Lorentz force is also conservative. Fig. 8b and d show that the current values used to calculate the Lorentz force based on Schemes II and IV are not conservative at the side layer. It seems that there are currents entering the side walls. The closed current streamline is not formed in the side layers. Scheme III (Fig. 8c) cannot

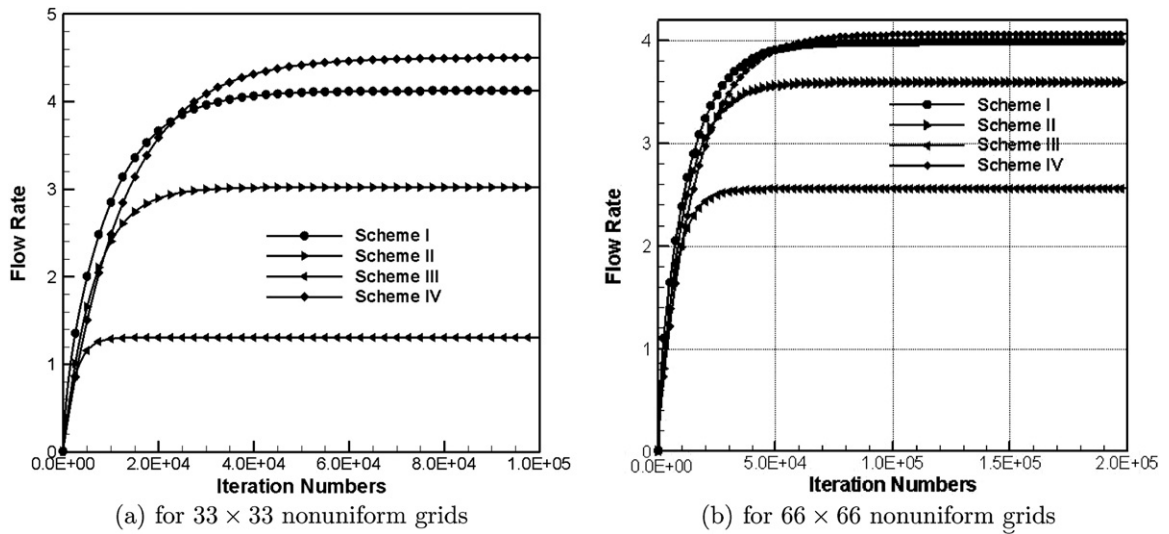


Fig. 5. Iteration history of flow rate using different schemes.

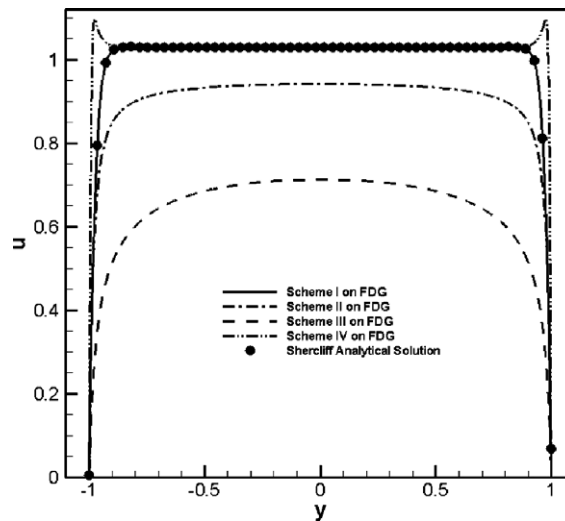


Fig. 6. Velocity distribution using different schemes on a  $66 \times 66$  non-uniform grid.

form a closed streamline too. Although Fig. 7 shows that Scheme III can locally conserve the current density in a control volume, the current at the cell centers used to calculate the Lorentz force is not conservative because of the non-conservative interpolation. Scheme III redistributes the current density in both directions. This redistribution can locally conserve the current density in a controlled volume, but is not physically correct. The current density leaves out of the wall from the side layer.

Although the current fluxes on the faces of a control volume from Scheme III is divergence free, the Lorentz force at the cell center is not calculated based on a conservative current. Therefore, Scheme III cannot get an accurate result either. Velocity contours are shown in Fig. 9 from the fine mesh with  $66 \times 66$  non-uniform grids. As we have already seen in Fig. 6, Scheme II and Scheme III give a lower velocity in the core flow, while Scheme IV gives a result with a velocity jump in the side layers. These are due to non-conservative current distribution from the inconsistent and non-conservative schemes.

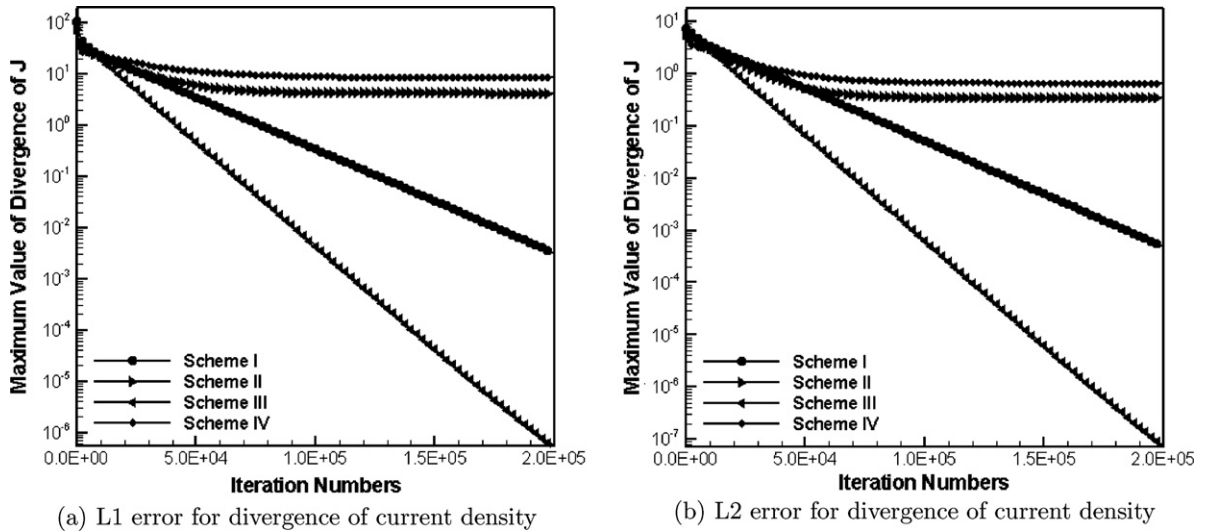


Fig. 7. Iteration history of divergence of current density.

Generally speaking, the current fluxes on the cell face calculated using the consistent scheme are locally conservative in a control volume as shown in Fig. 7 for Schemes I and III. And the current densities at the cell centers interpolated from the conservative current fluxes on the cell faces are conservative as shown in Fig. 8 for Scheme I. Only conservative current densities at the cell centers can be used for the calculation of the Lorentz force with accurate results as shown in Fig. 9 for Scheme I. The inconsistent schemes for the current fluxes and the non-conservative interpolation from the cell faces to cell centers cannot get a good result for MHD flows at a high Hartmann number as shown in Fig. 9 for Schemes II, III and IV.

#### 4.1.2. Order of accuracy

The order of accuracy of a numerical scheme is customarily computed based on a sequence of uniformly spaced meshes. The numerical solutions of high Hartmann number flows must usually involve severely stretched meshes. The use of uniform mesh spacing will result in an unduly large number of cells and unreasonable computational time. In the case of fully developed MHD flow in a square duct with insulating walls, the velocity in the core of the duct is fairly uniform, and it may be surmised that the numerical errors are caused largely in the Hartmann and side-layer regions. If these regions are resolved by uniform mesh spacing, a smoothly stretched mesh with much larger cells can be used in the core of the flow, thus, presumably, not affecting the order of accuracy of these calculations.

We generate a sequence of three meshes at each of the Hartmann numbers 50, 500 and 1000. These meshes use 4, 8 and 16 cells to resolve the Hartmann and side layers with a uniform spacing. This resolution is carried out to two times the conventional  $1/Ha$  thickness of the Hartmann layer and  $1/Ha^{1/2}$  thickness of the side layer, and smoothly increased towards the core. The core of the channel is resolved by using 30 cells in each direction for all cases. This results in mesh sizes of  $38 \times 38$ ,  $46 \times 46$  and  $62 \times 62$  for each Hartmann number. Fig. 10 shows sample meshes for  $Ha = 500$ .

We compute the  $L1$  and  $L2$  error norm in the solution from the following expressions, noting that the exact solution to this problem is known.

$$\|\varepsilon\|_{L1} = \int_{\Omega} |u - u_{\text{exact}}| d\Omega, \|\varepsilon\|_{L2} = \int_{\Omega} (u - u_{\text{exact}})^2 d\Omega \quad (86)$$

From the slopes of the logarithm of error vs. representative mesh size, a formal order of accuracy can be computed from the above data. The actual mesh size is a proportionality factor that appears as an additive constant in the logarithmic data above. The ratio of each mesh size against the subsequent mesh size is  $1 : \frac{1}{2} : \frac{1}{4}$ . Table 1 shows the computed order from this data. Interestingly, we observe that the actual  $L1$  and  $L2$  error

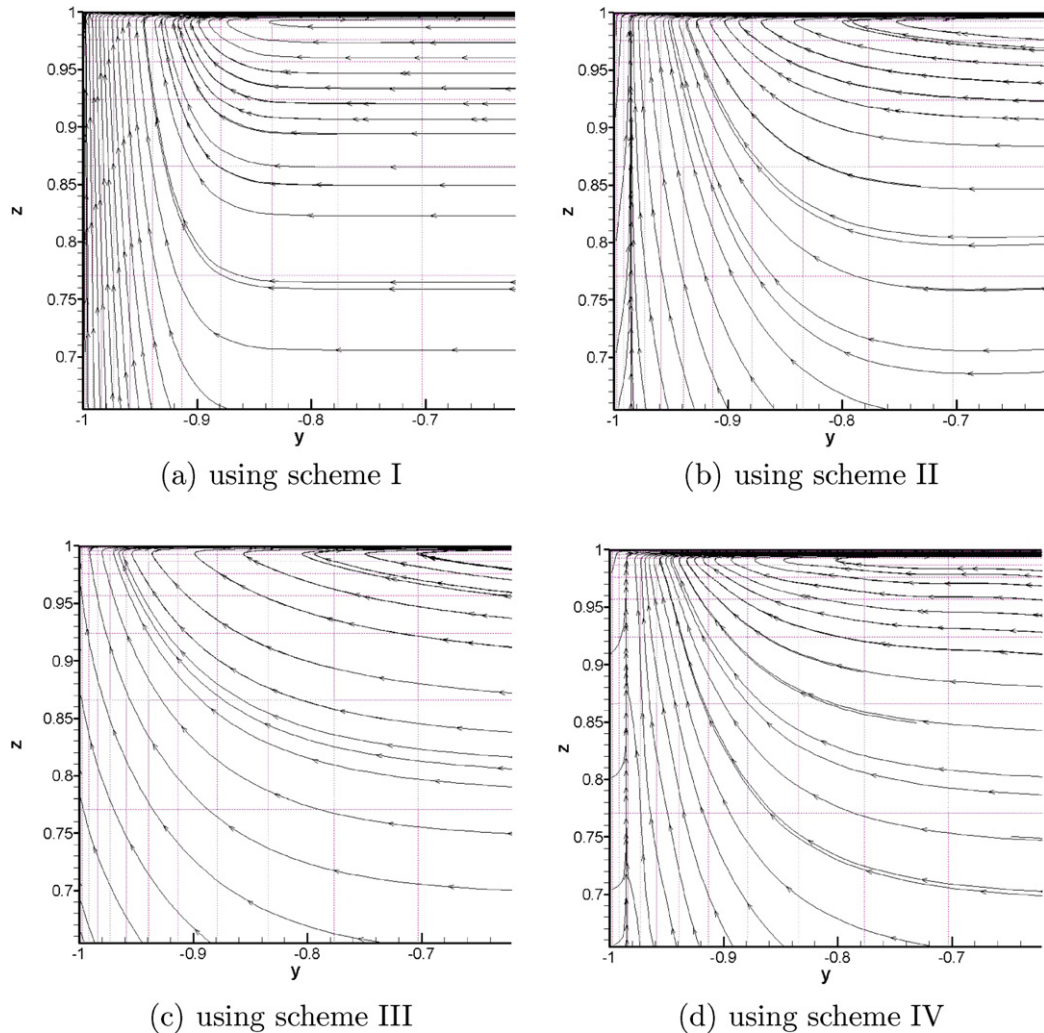


Fig. 8. Current density inside the side wall layer with  $33 \times 33$  grid numbers.

at each mesh level is approximately the same for all Hartmann numbers. This is perhaps due to the fact that the mesh has been chosen to exactly resolve the regions of gradients and that the velocity profile has been sized to yield the same mass flow rate and thus the same mean flow speed in all cases.

We observe a trend of numerical order decreasing slightly with increasing Hartmann number. This can be caused both by the greater stretching factors at higher Hartmann numbers, as well as the tendency of numerical errors to grow proportionate to an exponent of the Hartmann number in such calculation, thus causing a singular perturbation-type effect in numerical accuracy. For reference, we provide here a table of converged mass flow rates (see Table 2) from computed solutions for the various Hartmann numbers and grids used. Pressure gradient used in the calculation was selected such that the exact value of the mass flow rate is 4.

Also, the fact that the grid number in the core flow does not increase with Hartmann number may reduce the test accuracy.

#### 4.2. Hunt's case

The projection method of Eqs. (12)–(15) for the incompressible MHD equations and the consistent and conservative schemes for the calculation of the current density and the Lorentz force have been implemented into a parallel 3D code of HIMAG [38], which is used to conduct the following numerical simulations.

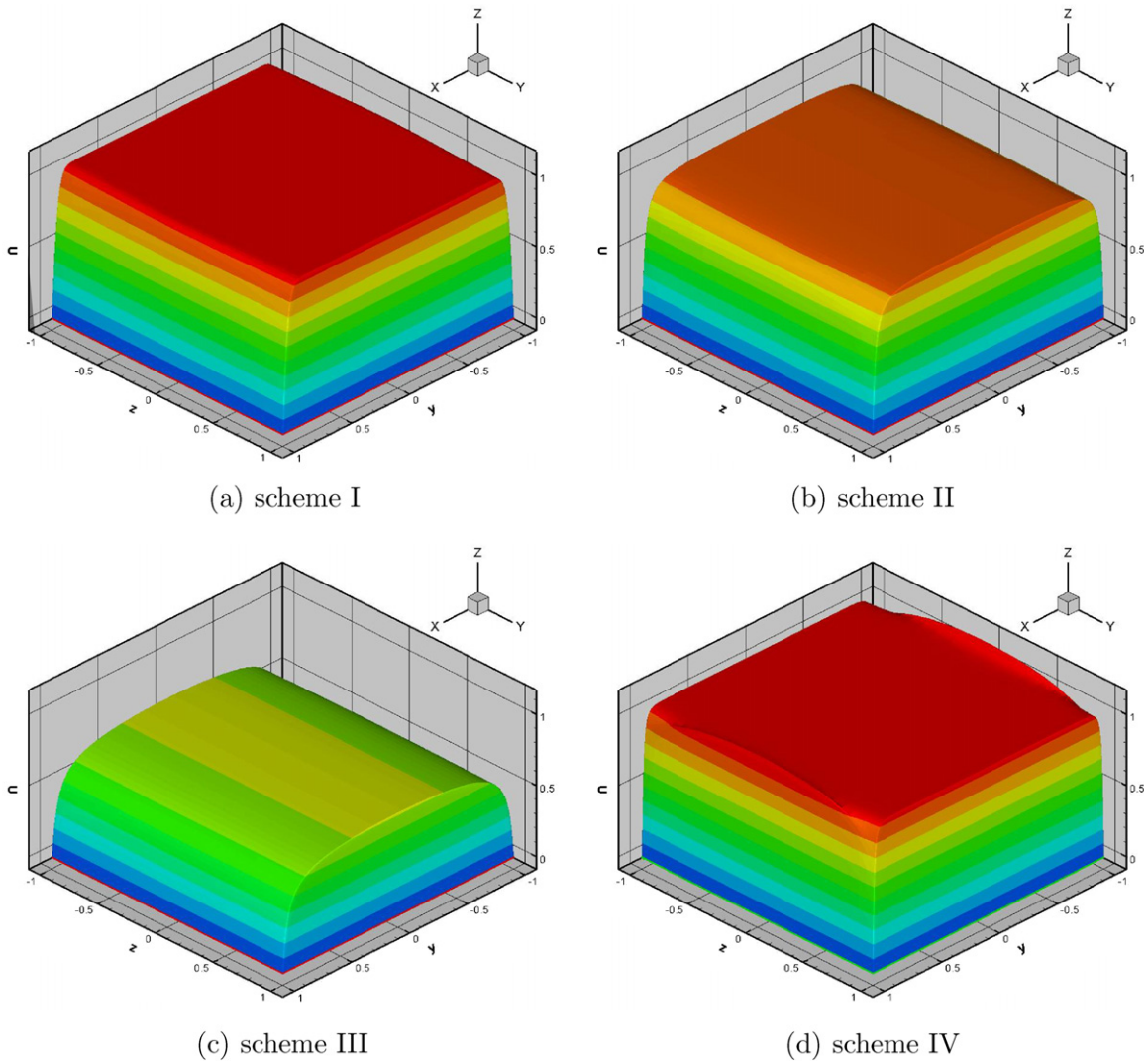


Fig. 9. Velocity contours on a  $66 \times 66$  non-uniform grid.

#### 4.2.1. Fully developed flow

We begin by considering fully developed flow at  $Re = 10$  (with characteristic velocity specified as 1),  $Ha = 300$ . The walls perpendicular to the applied magnetic field are assumed to be conducting and those parallel to the applied magnetic field are insulated. In the fully developed flow simulation, we make the assumption that the non-linear advection terms are negligible, and set Neumann boundary conditions on the velocity at the  $x$ -facing boundaries. In a fully developed region, the pressure gradient is constant. This constant pressure gradient is used as input data to get Hunt's analytical result. A pressure gradient of  $-300$  is specified. Fig. 11 shows the convergence history of the mass flow rate, peak velocity (Fig. 11a) and the converged velocity profile compared with Hunt's exact solution (Fig. 11b), converged velocity distribution (Fig. 11c) and current distribution (Fig. 11d). The velocity matches well with Hunt's analytical result.

#### 4.2.2. 3D simulations

It is certainly of interest to test our approach in a three-dimensional simulation. We choose here the same cross section as above and extend it in the  $x$ -direction to 30 units (channel half-width is 1). A non-uniform

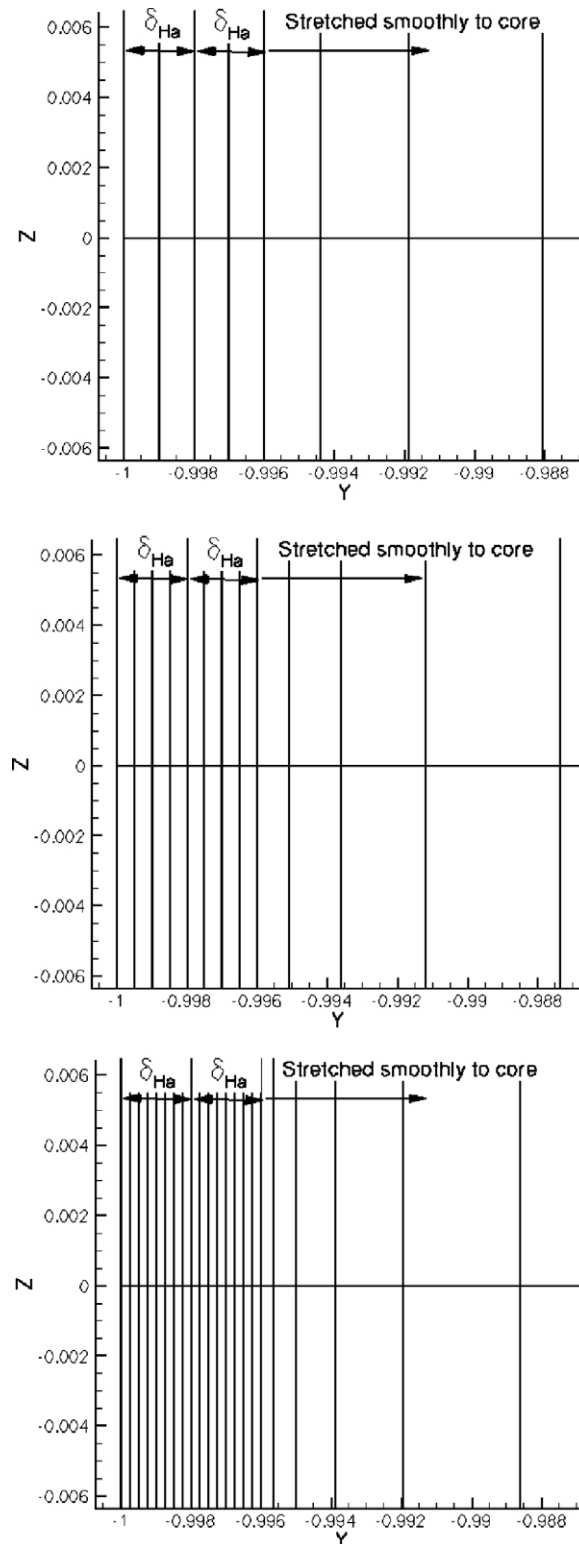
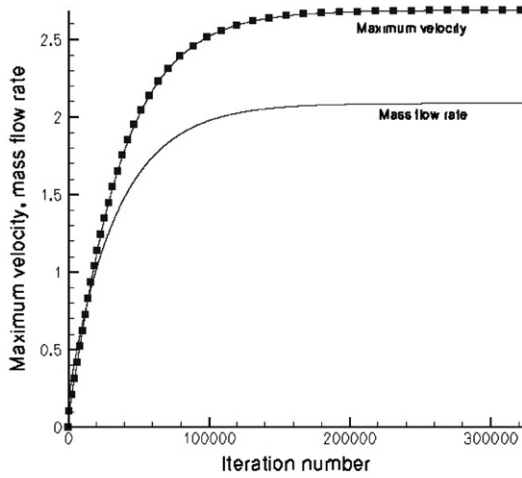


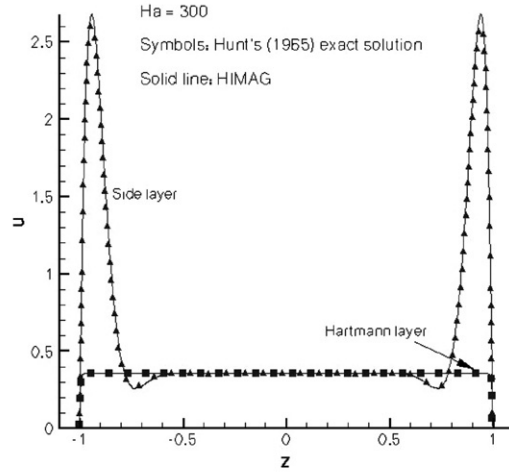
Fig. 10. Three meshes used in a computation of  $Ha = 500$  flow. From top to bottom, the dimension  $2/Ha$  is resolved by 4, 8 and 16 cells, respectively. Mesh is expanded smoothly to the interior, using 30 cells in all cases.

Table 1  
Computed order of accuracy

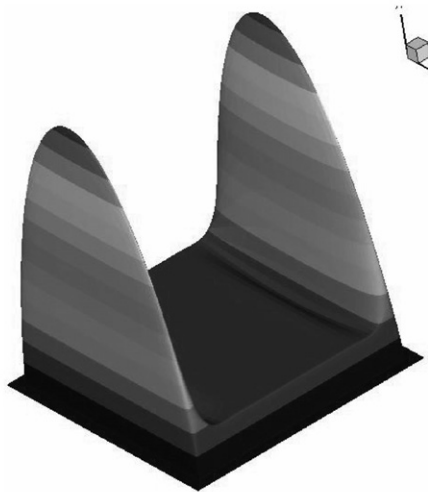
Hartmann number	L1 order	L2 order
50	1.8688	1.8580
500	1.8330	1.8277
1000	1.8155	1.8097



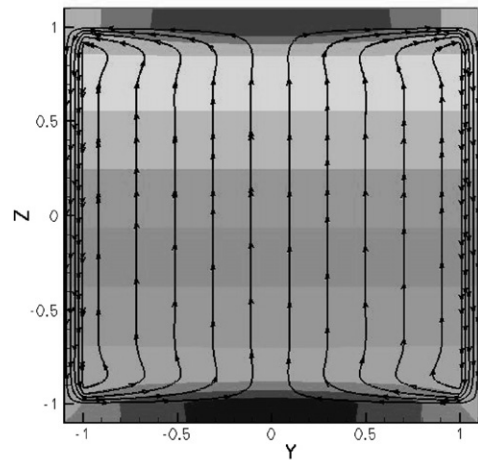
(a) convergence history of peak velocity and mass flow rate



(b) solution comparison



(c) velocity distribution



(d) current distribution

Fig. 11. Numerical results for Hunt's fully developed case with  $Ha = 300$ .

mesh containing  $31 \times 47 \times 47$  nodes and 63,480 cells was used in this simulation. The mesh is partitioned to run on 16 different processors.

A bi-parabolic inflow velocity distribution is given and used as an initial flow condition in the channel. Magnetic field with a value of 1 is applied in the  $y$ -direction. The flow quickly adjusts from ordinary laminar flow profile to the fully developed MHD state (Fig. 12a), converges rapidly, and is virtually indistinguishable

Table 2  
Computed mass flow rate

Hartmann number	Mesh-1	Mesh-2	Mesh-3
50	4.13534	4.03574	4.01075
500	4.14244	4.04400	4.01862
1000	4.13525	4.03927	4.01476

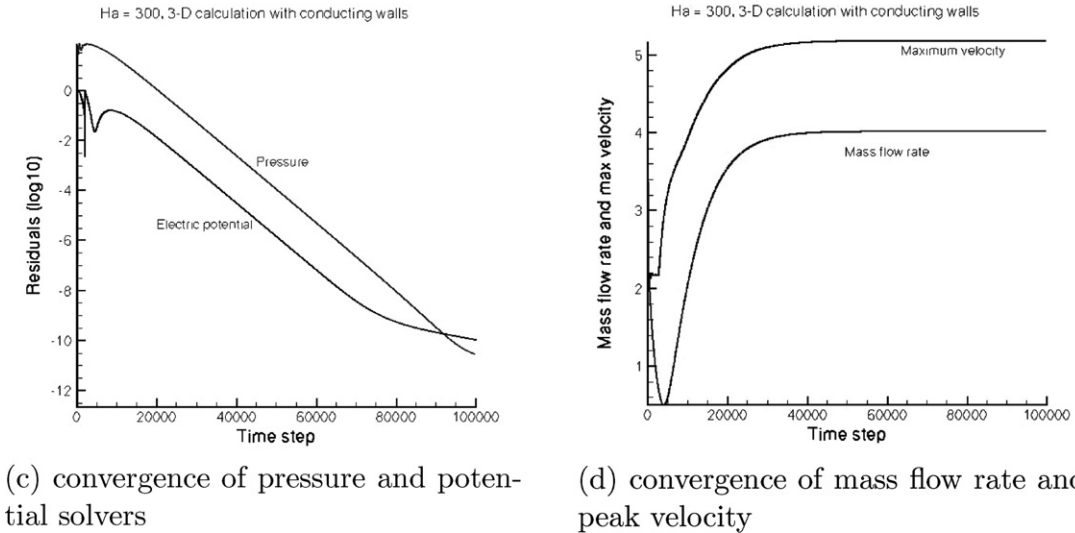
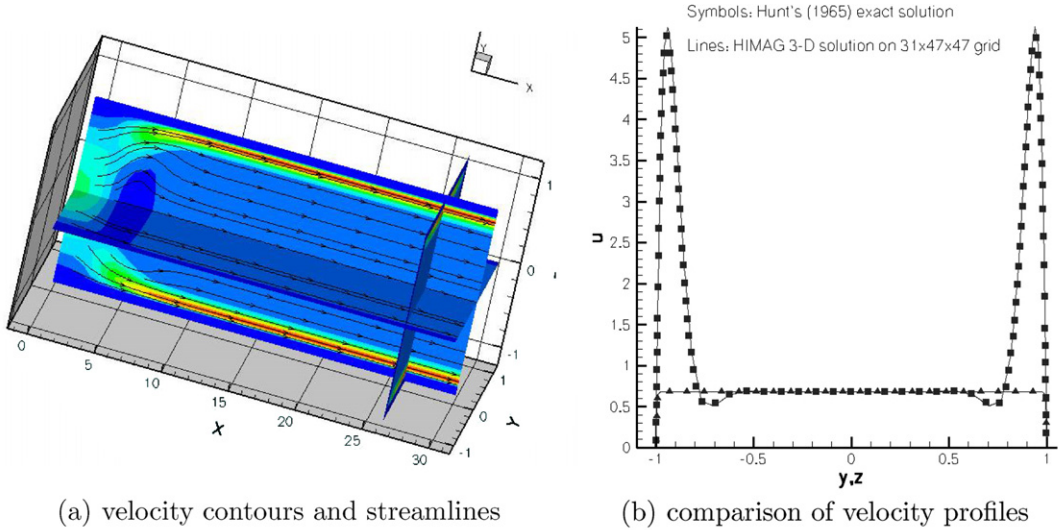


Fig. 12. 3D numerical solution for Hunt’s fully developed case with  $Ha = 300$ .

from the exact solution even for a relatively coarse mesh. These comparisons are shown in Fig. 12b. The pressure gradient is computed and used as an input to Hunt’s exact solution. Velocity profiles from both sources are compared and they match well. The convergence of maximum velocity and mass flow rate (Fig. 12d), and residuals of pressure and electrical potential are also shown in Fig. 12c. A dramatic correction to mass flow rate (dropping the error by several orders of magnitude) is seen to occur towards the end of the computation, when the Poisson equations for pressure and potential begin to show a tapering of their residual histories.

Table 3  
Computed pressure gradient at  $Ha = 300$  and  $c_w = 0.1$

Reynolds number	10	100	500	1000
Interaction parameter	9000	900	180	90
Calc. $\nabla p$	-585.0810	-58.50701	-11.70214	-5.858703
Anal. $\nabla p$	-585.4302	-58.54302	-11.70860	-5.854302
Calc. error	0.060%	0.062%	0.055%	0.075%

Table 4  
Computed pressure gradient at  $Ha = 500$  and  $c_w = 0.05$

Reynolds number	10	100	500	1000
Interaction parameter	25,000	2500	500	250
Calc. $\nabla p$	-952.57338	-95.280135	-19.065981	-9.5346676
Anal. $\nabla p$	-953.14475	-95.314475	-19.062895	-9.5314475
Calc. error	0.06%	0.036%	0.016%	0.033%

With  $Ha = 300$  and the conductance  $c_w = 0.1$ , we used the consistent and conservative scheme to do the direct calculation of 3D MHD flows at  $Re = 100$  ( $N = 900$ ),  $Re = 500$  ( $N = 180$ ) and  $Re = 1000$  ( $N = 90$ ). The inlet flow rate is fixed at 4. The calculated pressure gradients are given in Table 3 with analytical values listed in the table too. The relative error is calculated based on the following formula of  $\text{Error} = \left| \frac{(\nabla p)_{\text{Anal}} - (\nabla p)_{\text{Calc}}}{(\nabla p)_{\text{Anal}}} \right|$ . The calculated pressure gradients matches well with the analytical solution when the interaction parameters changed from 9000 to 90.

We also calculated the 3D MHD flows with  $Ha = 500$ ,  $c_w = 0.05$ . Again, the inlet flow rate is fixed at 4, and the calculated pressure gradients are listed in Table 4. The calculated pressure gradients match well with the analytical solution from low interaction parameter of 250 to high interaction parameter of 25,000 with relative error below 0.06%.

#### 4.2.3. A case study at $Ha = 10,000$

We present here some observations on the calculation of  $Ha = 10,000$  and  $Re = 1000$  flow in a square duct. This is a large Hartmann number by the standard of MHD simulation in 3D. We experimented with fully

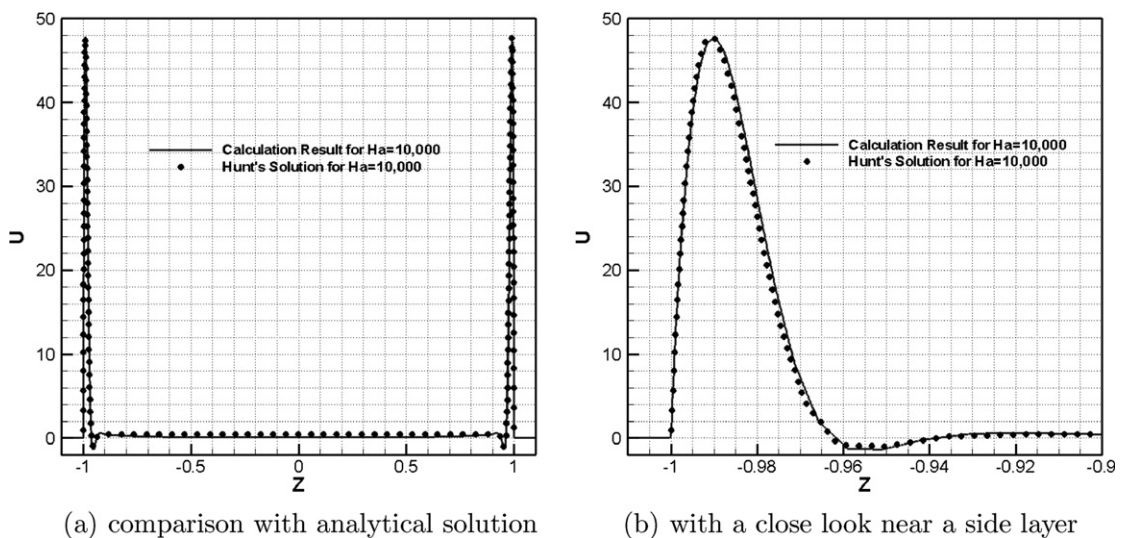
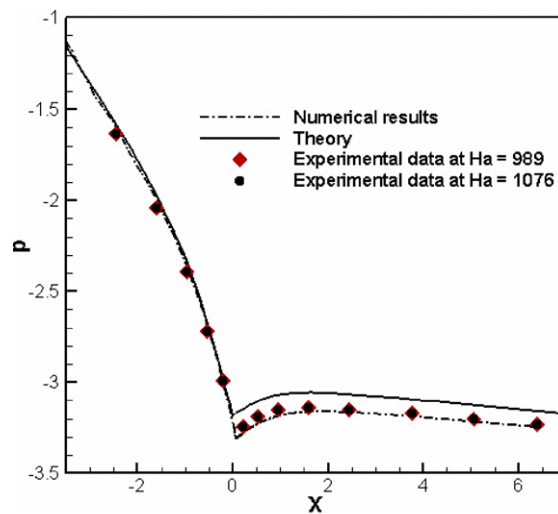


Fig. 13. Computed velocity profile and current lines for fully developed flow at  $Ha = 10,000$ ,  $Re = 1000$  in a square duct with conducting Hartmann walls with  $c_w = 0.05$  and insulating side-walls.

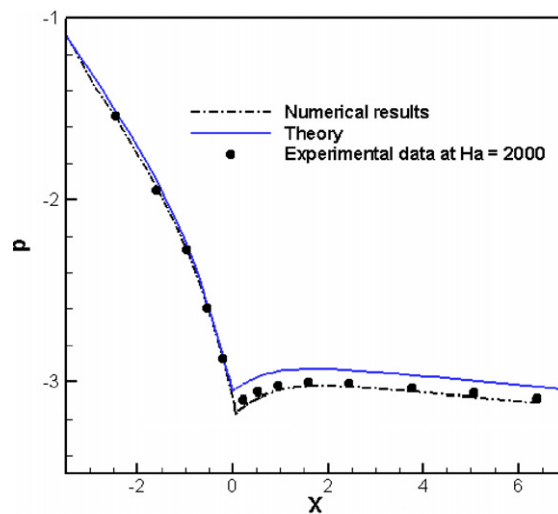
developed flow calculations in the cross section, as well as the three-dimensional developing flow situation. A channel of dimensions  $2 \times 2$  was padded with walls with a thickness of 0.1 on all sides. The mesh has  $67 \times 67$  cells in the cross section with 4 cells in the Hartmann layer. The grid on a cross section generated for Hartmann number of 10,000 is shown in Fig. 2. The 3D mesh uses 20 mesh points over a length of 20 units. Magnetic field with a value of 1 is applied. Pressure is held fixed at the exit plane, while the electric potential is held fixed at the inflow. The Hartmann walls are assumed to be conducting with a wall conductance ratio  $c_w = 0.05$  and the side-walls are insulated.

The 3D case used a fixed mass flow rate of 4 at the inflow, specified as a bi-parabolic profile. This simulation is performed on a parallel cluster with 16 processors. The convergent pressure gradient of 1990.62 was observed in the fully developed region, which is very close to the Hunt's analytical result of 1972.26.

Fig. 13a gives the comparison between our results at the fully developed region and Hunt's analytical results. Fig. 13b zooms in the side layer. The numerical results from the consistent and conservative schemes on a collocated non-uniform grid match very well with Hunt's solution. The figure clearly shows the M-shape formed by the Lorentz force. In fact, we can see that two jets form in the side layers. The turbulence due to the



(a) for  $Ha = 1000$ ,  $Re = 1000$



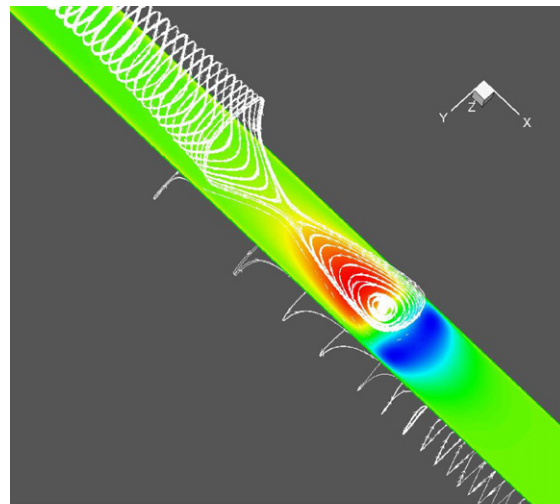
(b) for  $Ha = 2000$ ,  $Re = 2000$

Fig. 14. Pressure along the upper Hartmann wall.

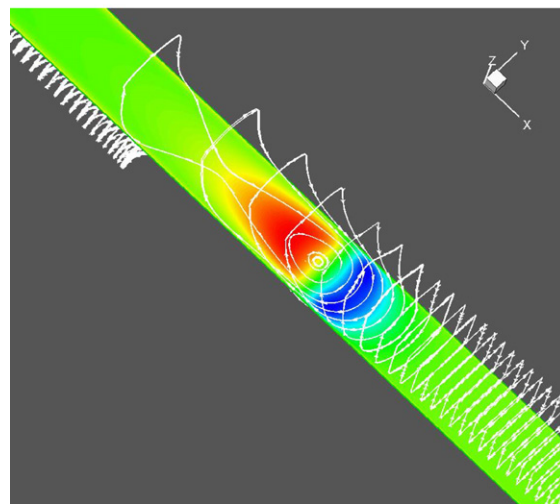
high velocity in the jet has been studied in [39], which can be an interesting future direction of research using our approach.

#### 4.3. Application to 3D MHD flows with conductive walls

Experiments on MHD flows in a conducting rectangular channel with a sudden expansion have been performed recently by Bühler and Horanyi [40]. We simulated these experiments using the current density consistent and conservative scheme. Here we compare the pressure distribution along the upper Hartmann wall. Fig. 14a compares our calculated pressure distribution with the theoretical value (which is a core flow asymptotic solution as  $N \rightarrow \infty$ ) and the experimental data at  $Ha = 1000$  and  $N = 1000$ , while Fig. 14b compares at  $Ha = 2000$  and  $N = 2000$ . The calculated pressure distribution matches well with the experimental data. The numerical results [30] for a fully 3D MHD flows in a circular pipe with conductive walls using the current density conservative scheme on an unstructured grid also match well with the available experimental data. These indicate that the consistent and conservative scheme can be used to accurately simulate the MHD flows with full conducting walls.



(a) from inlet



(b) to exit

Fig. 15. Three dimensional current streamlines with plot size ratio 1:1:15.

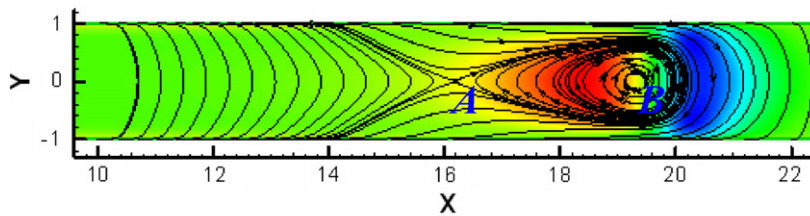
4.4. Application to 3D MHD flow with fringing magnetic field

A fringing (spatially varying) external magnetic field can induce a three-dimensional MHD flows [14,42] [43]. Numerical simulations using the full set of MHD equations without simplifications have been performed. The applied normalized fringing magnetic field is given as follows [44]:

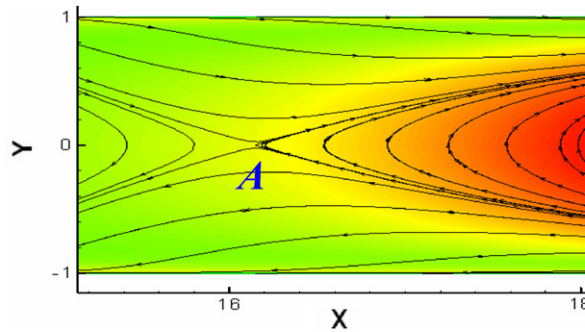
$$B_x = \frac{\pi}{2}zB^2(1 - B^2), \quad B_y = 0, \quad B_z = B - \frac{z^2\pi^2}{4}B^3(1 - B^2)(1 - 2B^2) \tag{87}$$

with  $0 \leq x \leq 40$ ,  $-1 \leq y \leq 1$ , and  $-0.2 \leq z \leq 0.2$ . The parameter  $B$  in the above equations is given by the following implicit function of the variable  $x$ , and will be numerically solved:

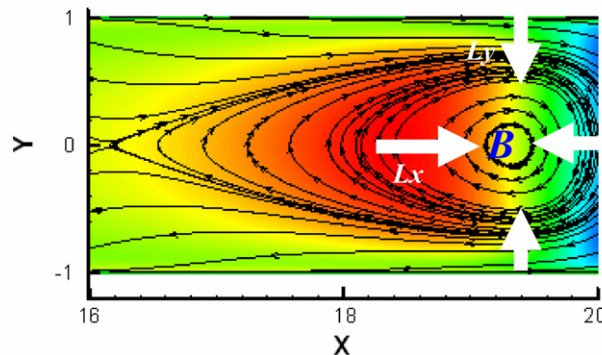
$$F(B, x) = \frac{2}{\pi} \left( \frac{1}{B} + 0.5 \ln \left( \frac{1-B}{1+B} \right) \right) + (x - x^*) = 0 \tag{88}$$



(a) current streamlines around the fringing area



(b) saddle point at  $x = 16.1399$

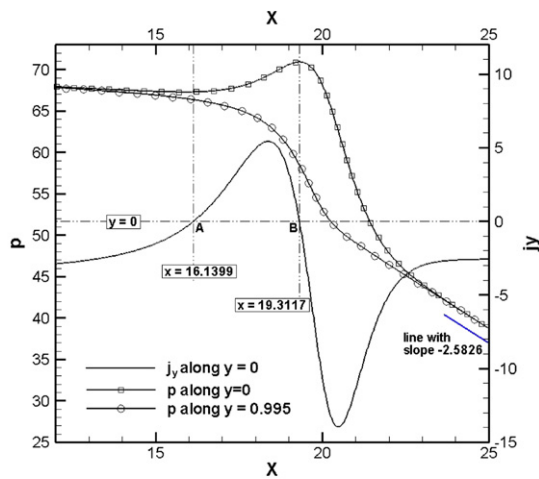


(c) closed loops with center at  $x = 19.3117$ , schematic Lorentz force

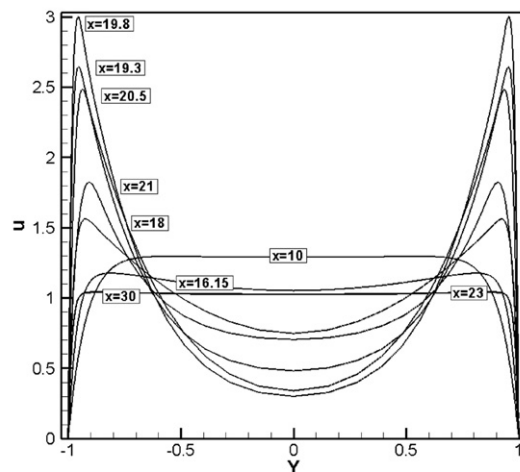
Fig. 16. Current streamline at plane of  $z = 0$  around the fringing area.

Around  $x = x^*$ , there is a large magnetic field gradient from Eq. (88). The applied magnetic field is nearly curl free with a small error and exactly divergence free. In this simulation, we take  $Ha = 100$  and  $Re = 200$ , the inertial effect is not negligible, and the applied magnetic field is along two directions.

The current paths are depicted in Fig. 15. Downstream at some distance from the fringing, the current distribution corresponds to fully developed conditions; the current loops are 2D, and they close in cross-sectional planes. Upstream does not correspond exactly to a fully developed condition, since the applied magnetic field of  $B_z$  is not constant at the inlet; we can also see a weak axial current density here. However, approaching the fringing, the current loops clearly incline in the direction of the motion due to the presence of induced axial currents. The path that encloses the zone shows strong three-dimensional effects. A schematic figure is given to represent the pattern in Fig. 16a, in which current streamlines are plotted on the plane  $z = 0$ . There are current lines that surround the area in which core loops develop. Some of these current streamlines, after entering the fringing area, move to the middle of the channel before again approaching the side walls. The point where the current line narrows, close to the center of the duct, can be interpreted as a saddle point, marked as A in Fig. 16a, and clearly shown in Fig. 16b. It indicates the location where the transverse component of current



(a) pressure along  $y = 0$  and  $y = 0.995$ , current  $J_y$  along  $y = 0$



(b) Velocity in flow direction at the plane of  $z = 0$  and at different cross section

Fig. 17. Pressure and velocity distributions verse to  $x$  at the plane of  $z = 0$ .

density  $J_y$  starts flowing again in the direction of the 2D currents. The trace of core current loops with center marked as  $B$  is shown in Fig. 16a and c. The saddle point and closed loops are also found in the three-dimensional MHD flow of a sudden expansion in [24].

The transverse component of current density  $J_y$  along the line of  $y = 0$  and  $z = 0$  has been illustrated in Fig. 17a. The line  $J_y = 0$  has two intersections with the curve, which are marked as  $A$  and  $B$ .  $A$  represents the saddle point, and  $B$  represents the current core loops' center, respectively, which have been illustrated in Fig. 16c. The pressure and velocity distributions along the line of  $y = 0$  at the plane of  $z = 0$  has also been given in Fig. 17a. In the fully developed region, the pressure distribution has a constant gradient. In the fringing region, the pressure reaches the peak value at the center of the closed current loops shown in Fig. 16c. The velocity reaches its lowest value a little distance from the center. This is partly due to the contribution of the axial component of the current density. The local current density distribution with components in flow direction results in Lorentz forces with direction towards the center. The positive value of  $J_y$  distribution between the saddle point  $A$  and the closed loops' center  $B$ , the negative value of  $J_y$  outside of this region will make the Lorentz force acting toward the center  $B$ . The schematic Lorentz force directions acting around the center are also illustrated in Fig. 16c. The Lorentz force acting around the center of the closed loops from four directions results in a peak value of pressure at the center of  $B$ . As a consequence, a high transversal pressure gradient is induced, as shown in Fig. 17a. In this figure, the pressure distribution along  $y = 0$  and along  $y = 0.995$  at the plane of  $z = 0$  are shown. In the fringing area, the pressure along  $y = 0$  is higher than it is along  $y = 0.995$  (inside the Hartmann layer) due to the contribution of the axial component of current density. The pressure at  $y = 0$  is reduced greatly after it reaches a peak value at the center of the closed loops, which is due to the large negative value of  $J_y$  shown in Fig. 17a. In the fully developed region, the pressure gradient and the transversal component  $J_y$  of the current density have constant negative values.

Moreover, the pressure gradient around the closed loops' center  $B$  will decelerate the core flow upstream and accelerate it downstream. And the highest pressure at the closed loops' center expels the flow from the core flow region of the duct to the vicinity of the side walls, generating significant overspeed and an overall M-shaped velocity profile. Fig. 17b shows the velocity distribution in a rectangular duct, calculated near the center and near the side. In the region where the magnetic field varies, the velocity is strongly reduced in the center, while it increases near the side.

## 5. Conclusions

A general second-order projection method has been developed for incompressible Navier–Stokes equations with the Lorentz force included. This method can balance the pressure gradient and the Lorentz force for a fully developed core flow and simplifies boundary conditions for the pressure. A consistent and conservative scheme has been designed for the calculation of the current density and the Lorentz force on a collocated rectangular grid. The consistent method can ensure the calculated current fluxes divergence free in a control volume. The current density at a cell center needed to calculate the Lorentz force is determined using a conservative interpolation from the fluxes at the cell faces. It is also demonstrated that only conservative current at the cell center can be used to accurately calculate the Lorentz force. This projection method and the consistent and conservative scheme have been applied for MHD flows at high Hartmann numbers. The current density consistent and conservative scheme can be applied to do direct simulations of MHD at low magnetic Reynolds number with high or low Hartmann numbers, with or without strong inertial terms, with conducting or insulated walls. It is also extended for MHD flows in a complicated geometry on an arbitrary unstructured collocated grid system [30], in which a fully conservative formulation of the Lorentz force has been employed to conduct the simulation. Future work including simulations of unsteady MHD flows with parallel algorithms and advanced accelerated techniques employed will be conducted using the current density conservative scheme.

## Acknowledgments

The authors from UCLA acknowledge the support from the US Department of Energy under Grant # DE-FG03-86ER52123, and the authors from HyperComp Inc. acknowledge the support from the US Department

of Energy under DOE SBIR Grant # DE-FG02-04ER83977. M.-J. acknowledges the discussion with Dr. Sergey Smolentsev and his interesting in the simulation of 3D MHD flows with fringing applied field. The experimental data of 3D MHD flows in a sudden expansion is from Leo Bühler.

## References

- [1] M.A. Abdou et al., On the exploration of innovative concepts for fusion chamber technology fusion, *Fusion Engineering and Design* 54 (2001) 181–247.
- [2] N.B. Morley, S. Smolentsev, R. Munipalli, M.-J. Ni, D. Gao, M.A. Abdou, Progress on the modeling of liquid metal, free surface, MHD flows for fusion liquid walls, *Fusion Engineering Design* 72 (2004) 3–34.
- [3] S. Malang et al., Self-cooled liquid–metal blanket concept, *Fusion Technology* 14 (1988) 1343–1356.
- [4] M.A. Abdou, D. Sze, C. Wong, M. Sawan, A. Ying, N.B. Morley, S. Malang, US Plans and strategy for ITER blanket testing, *Fusion Science and Technology* 47 (2005) 475–487.
- [5] L. Bühler, The influence of small cracks in insulating coatings on MHD and heat transfer in rectangular ducts, *Fusion Engineering and Design* 27 (1995) 634–641.
- [6] J.A. Schercliff, The flow of conducting fluids in circular pipes under transverse magnetic fields, *Journal of Fluid Mechanics* 1 (1956) 644.
- [7] J.A. Schercliff, Steady motion of conducting fluids in pipes under transverse magnetic fields, *Proceedings of the Cambridge Philosophical Society* 49 (1953) 126–144.
- [8] J.C.R. Hunt, Magnetohydrodynamic flow in rectangular ducts, *Journal of Fluid Mechanics* 21 (1965) 577–590.
- [9] J.S. Walker, Magnetohydrodynamic flow in rectangular ducts with thin conducting walls, *Journal de Mécanique* 20 (1981) 79.
- [10] A.G. Kulikovskii, Slow steady flows of a conducting fluid at large Hartmann numbers, *Fluid Dynamics* 3 (1968) 1–5.
- [11] L. Bühler, Magnetohydrodynamic flows in arbitrary geometries in strong, non-uniform magnetic fields – a numerical code for the design of fusion reactor blankets, *Fusion Technology* 27 (1994) 3–24.
- [12] S. Molokov, L. Bühler, Liquid metal flow in a U-bend in a strong uniform magnetic field, *Journal of Fluid Mechanics* 267 (1994) 325–352.
- [13] R.J. Moreau, *Magnetohydrodynamics*, Kluwer Academic Publishers., 1990.
- [14] U. Müller, L. Bühler, *Magnetofluidynamics in Channels and Containers*, Springer, 2001.
- [15] P.A. Davidson, *An Introduction to Magnetohydrodynamics*, Cambridge University Press, 2001.
- [16] A. Sterl, Numerical simulation of liquid–metal mhd flows in rectangular ducts, *Journal of Fluid Mechanics* 216 (1990) 161–191.
- [17] L. Leboucher, Monotone scheme and boundary conditions for finite volume simulation of magnetohydrodynamic internal flows at high Hartmann number, *Journal of Computational Physics* 150 (1999) 181–198.
- [18] Y. Morinishi, T.S. Lund, O.V. Vasilyev, P. Moin, Fully conservative higher order finite difference schemes for incompressible flow, *Journal of Computational Physics* 143 (1998) 90–124.
- [19] O.V. Vasilyev, High order finite difference schemes on non-uniform meshes with good conservation properties, *Journal of Computational Physics* 157 (2000) 746–761.
- [20] B. Perot, Conservation properties of unstructured staggered mesh scheme, *Journal of Computational Physics* 159 (2000) 58–89.
- [21] K. Mahesh, G. Constantinescu, P. Moin, A numerical method for large eddy simulation in complex geometries, *Journal of Computational Physics* 197 (2004) 215–240.
- [22] Y. Shimomura, Large eddy simulation of magnetohydrodynamics turbulent channel flows under a uniform magnetic field, *Physics of Fluids A* 3 (1991) 3098.
- [23] N. Umeda, M. Takahashi, Numerical analysis for heat transfer enhancement of a lithium flow under a transverse magnetic field, *Fusion Engineering and Design* 51–52 (2000) 899–907.
- [24] C. Mistrangelo, *Three-Dimensional MHD Flow in Sudden Expansion*, Ph.D Thesis, der Fakultät für Maschinenbau, der Universität Karlsruhe, 2005.
- [25] I.D. Piazza, L. Bühler, A general computational approach for MHD flows using the CFX Code: buoyant flow through a vertical square channel, *Fusion Technology* 38 (2000) 180–189.
- [26] S. Aleksandrova, S. Molokov, C.B. Reed, *Modeling of Liquid Duct and Free-Surface Flows Using CFX*, ANL/TD/TM02-30, 2003.
- [27] ANSYS CFX Home, <http://www-waterloo.ansys.com/>.
- [28] C.M. Rhie, W.L. Chow, A numerical study of turbulent flow past an isolated airfoil with trailing edge separation, *AIAA Journal* 21 (1983) 1525–1532.
- [29] Y. Zang, R.L. Street, J.R. Koseff, A non-staggered grid, fractional step method for time-dependent incompressible Navier–Stokes equations in curvilinear coordinates, *Journal of Computational Physics* 114 (1994) 18–33.
- [30] M.-J. Ni, M.A. Abdou, A current density conservative scheme for high Hartmann MHD with low magnetic Reynolds number. Part 2. On unstructured grid system. *Journal of Computational Physics* for review, in press, doi:10.1016/j.jcp.2007.07.023.
- [31] M.J. Ni, M.A. Abdou, A bridge between Projection methods and SIMPLE type methods for incompressible Navier–Stokes Equations, *International Journal for Numerical Methods in Engineering*, in press, doi:10.1002/nme.2054.
- [32] J.B. Bell, P. Colella, H.M. Glaz, A second-order projection method for the incompressible Navier–Stokes equations, *Journal of Computational Physics* 85 (1989) 257.

- [33] H. Choi, P. Moin, Effects of the computational time step on numerical solutions of turbulent flow, *Journal of Computational Physics* 113 (1994) 1–4.
- [34] S.V. Patankar, D.B. Spalding, A Calculation procedure for heat, mass and momentum transfer in three-dimensional parabolic flows, *International Journal Heat and Mass Transfer* 15 (1972) 1787–1806.
- [35] S.V. Patankar, *Numerical Heat Transfer and Fluid Flow*, McGraw-Hill, New York, 1980.
- [36] J.P. Van Doormaal, G.D. Raithby, Enhancement of the SIMPLE method for predicting incompressible fluid flows, *Numerical Heat Transfer* 7 (1984) 147–163.
- [37] M.-J. Ni, M.A. Abdou, Temporal second-order accuracy of SIMPLE-Type methods for incompressible unsteady flows, *Numerical Heat Transfer, Part B* 46 (2005) 529–548.
- [38] R. Munipalli, S. Shankar, M.-J. Ni, N.B. Morley, N., Development of a 3D Incompressible Free Surface MHD Computational Environment for Arbitrary Geometries: HIMAG, DOE SBIR Phase-II Final Report, 2003.
- [39] L. Bühler, Instabilities in quasi-2-dimensional magnetohydrodynamic flows, *Journal of Fluid Mechanics* 326 (1996) 125.
- [40] L. Bühler, S. Horanyi, Experimental Investigations of MHD flows in a Sudden Expansion, FZKA 7245, Forschungszentrum Karlsruhe, 2006.
- [42] C.B. Reed, B.F. Picologlou, T.Q. Hua, J.S. Walker, ALEX results – a comparison of measurements from a round and a rectangular duct with 3D code predictions, in: 12th Symposium on Fusion Engineering, Monterey, CA, October, 1987.
- [43] T.Q. Hua, B.F. Picologlou, C.B. Reed, J.S. Walker, MHD thermal hydraulic analysis of three-dimensional liquid–metal flows in fusion blanket ducts, *Fusion Engineering and Design* 8 (1989) 241–248.
- [44] S. Smolentsev, R. Moreau, private communication.